Structural features of heteromeric channels composed of CALHM2 and CALHM4 paralogs

Katarzyna Drożdżyk[1], Martina Peter[1] and Raimund Dutzler[1*]

[1]Department of Biochemistry, University of Zurich, Zurich, Switzerland

*For correspondence: dutzler@bioc.uzh.ch (RD)

Abstract

The CALHM proteins constitute a family of large pore channels that contains six closely related paralogs in human. Two family members, CALHM1 and 3, have been associated with the release of ATP during taste sensation. Both proteins form heteromeric channels that activate at positive potential and decreased extracellular Ca^{2+} concentration. Although the structures of several family members displayed large oligomeric organizations of different size, their function has in most cases remained elusive. Our previous study has identified the paralogs CALHM2, 4 and 6 to be highly expressed in the placenta and defined their structural properties as membrane proteins exhibiting features of large pore channels with unknown activation properties (Drozdzyk et al., 2020). Here we investigated whether these placental paralogs would form heteromers and characterized heteromeric complexes consisting of CALHM2 and CALHM4 subunits using specific binders as fiducial markers. Both proteins assemble with different stoichiometries with the largest population containing CALHM2 as predominant component. In these oligomers, the subunits segregate and reside in their preferred conformation found in homomeric channels. Our study has thus revealed the properties that govern the formation of CALHM heteromers in a process of potential relevance in a cellular context.

Introduction

Large pore channels encompass a heterogeneous group of membrane proteins in higher eukaryotes, which form large oligomeric assemblies that facilitate the diffusion of diverse substrates with poor selectivity, including metabolites and signaling molecules such as the nucleotide ATP (Syrjanen et al., 2021). The calcium homeostasis modulators (CALHM) constitute one family of large pore channels that contains six members in humans (Ma et al., 2016). Their role in physiology is currently best understood for the paralogs CALHM1 and 3. Both proteins are expressed in type II taste bud cells to contribute to the sensation of umami, sweet and bitter taste (Ma et al., 2018b; Taruno et al., 2013b). There, they are involved in the non-vesicular release of ATP as a consequence of membrane depolarization following the initial sensation of tastants by G-protein coupled receptors (Taruno et al., 2013a). ATP in turn acts as neurotransmitter to activate P2X-receptors on the postsynaptic side. CALHM proteins reside in a non-conducting state at resting potentials and are activated in response to membrane depolarization with a decrease in extracellular Ca^{2+} shifting the threshold of activation towards more hyperpolarizing voltages, thereby allowing conduction also at negative potentials (Ma et al., 2012). The open channel shows poor selectivity and is permeable to the multivalent anion ATP. Although these properties are shared by homomeric assemblies of CALHM1 in heterologous expression systems, their slow kinetics of activation would prohibit fast signaling and thus does not reflect the behavior observed in taste bud cells (Ma et al., 2012). To enhance its activation properties, CALHM1 assembles as heteromeric complex with its paralog CALHM3, which on its own does not form functional ion channels (Ma et al., 2018b). The physiological role of other CALHM paralogs is currently much less well understood, although the ubiquitously expressed CALHM2 was also associated with ATP

release (Liao et al., 2023; Ma et al., 2018a) and CALHM6 was recently described as channel in immunological synapses of macrophages (Danielli et al., 2023).

Based on their assumed topology containing four membrane-spanning segments, the CALHM family was originally predicted to share a close structural relationship with large pore channels of the connexin, pannexin and LRRC8 families (Siebert et al., 2013). However, this relationship was refuted in numerous structures of homomeric assemblies of different CALHM paralogs that have recently been determined by cryo-electron microscopy (cryo-EM) from samples obtained from heterologous expression in mammalian and insect cell culture (Choi et al., 2019; Demura et al., 2020; Drozdzyk et al., 2020; Foskett, 2020; Liu et al., 2020; Ren et al., 2022; Ren et al., 2020; Syrjanen et al., 2020; Yang et al., 2020). Although sharing the same number of membrane-spanning segments, their arrangement is unique and differs from other large pore channels, with an extended helix located on the C-terminus and forming the core of a cytoplasmic domain further mediating subunit interactions. These structures show channels that assemble into higher oligomers around an axis of symmetry that presumably defines the conduction path. These assemblies are heterogeneous in nature, with paralogs frequently adopting different oligomeric states in the same sample. The smallest assemblies were generally observed for CALHM1, where structures from different species contained between seven and nine subunits (Demura et al., 2020; Ren et al., 2022; Ren et al., 2020; Syrjänen et al., 2023; Syrjanen et al., 2020). The size of the respective assemblies is generally larger for other CALHM paralogs, ranging from decamers to tridecamers (Choi et al., 2019; Drozdzyk et al., 2020; Liu et al., 2020; Syrjanen et al., 2020). In detergent solution, these channels do in certain cases pair to form gap-junction like organizations, although there is currently no evidence for such transcellular interactions in a physiological environment (Choi et al., 2019; Syrjanen et al., 2020). In oligomeric channels, the pore is lined by

69 the first transmembrane segment (TM1) of each subunit, which forms an inner, of two concentric
70 rings, with the outer ring being constituted by TM2-4, with TM2 and 4 of neighboring subunits
71 engaging in extended interactions (Choi et al., 2019; Drozdzyk et al., 2020; Liu et al., 2020;
72 Syrjanen et al., 2020). The loosely packed TM1 is found in distinct conformations in different
73 structures to shape the pore geometry and thus presumably alter conduction properties (Choi et al.,
74 2019; Drozdzyk et al., 2020).
75 We have previously studied the structural and functional properties of the CALHM paralogs 2, 4
76 and 6, whose transcripts were found to be abundant in placental epithelia in dependence of the
77 developmental stage of the organ (Drozdzyk et al., 2020). These placental paralogs all form large
78 oligomers, which in CALHM4 consists of similar sized populations of decameric and undecameric
79 assemblies in the same sample. Both oligomers were found to pair via contacts on their intracellular
80 side into large tubular structures. In this sample, both assemblies adopt a similar subunit
81 conformation, leading to large cylindrical pores that are constricted by a short N-terminal helix
82 preceding TM1, which is oriented parallel to the membrane plane and projects towards the pore
83 axis (Drozdzyk et al., 2020). In the same study, a similar pairing of channels containing between
84 11 and 12 subunits was also found for CALHM2, where the preferred orientation of the particles
85 within the sample has prevented a three-dimensional reconstruction at high resolution. In contrast,
86 no dimerization was detected in a CALHM6 preparation, where, although also existing as
87 undecamers, a decameric assembly was prevalent and thus better resolved. As consequence of a
88 conformational rearrangement of TM1, which has detached from its interaction with the rest of the
89 subunit, resulting in a higher mobility, the CALHM6 pore has adopted a conical shape with
90 decreasing diameter towards the intracellular side suggesting that it might reside in a different
91 functional state (Drozdzyk et al., 2020).

92 Despite the observed large assemblies, none of the three paralogs overexpressed in *X. laevis*
93 oocytes showed any activity in electrophysiology experiments under conditions where CALHM1
94 was conductive, regardless of their expression at the cell surface, suggesting that they may be
95 activated by different stimuli (Drozdzyk et al., 2020). This was unexpected in light of the distinct
96 conformations observed for CALHM4 and 6 and their large apparent pore diameter, which is
97 particularly pronounced in case of CALHM4. In this respect, it was remarkable to find continuous
98 density with bilayer-like features inside the pore of CALHM4, matching the hydrophobic character
99 of the pore lining, which might explain the lack of activity observed for this protein (Drozdzyk et
100 al., 2020). This density is not found in CALHM6, where the altered shape of the pore could not
101 accommodate a bilayer. The functional properties of placental CALHM paralogs thus remained
102 elusive.
103 Since the formation of heteromers composed of CALHM1 and 3 paralogs strongly altered the
104 functional properties of the respective homomers, we wondered whether the tree paralogs
105 expressed in the placenta would share a similar property and whether their heteromerization would
106 increase their activity under the investigated conditions. To clarify this question, we have here
107 investigated the ability of the overexpressed CALHM homologs 2, 4 and 6, to form heteromeric
108 assemblies. Robust interactions were identified between CALHM2 and 4, but to a much lower
109 extent between any of the two paralogs and CALHM6. The subsequent structural characterization
110 of CALHM2/4 heteromers, employing synthetic subunit-specific nanobodies (sybodies), showed
111 channels with a broad subunit distribution. Predominant species contain a predominance of
112 CALHM2 with two to four CALHM4 subunits, where both paralogs segregate in the heteromeric
113 assemblies. While subunits maintain their distinct structural features found in homomeric
114 channels, they also influence the conformations of contacting subunits.

115

116 **Results**

117 **Formation of CALHM heteromers**

118 The formation of heteromers is a hallmark of different eukaryotic ion channels, with their subunit
119 composition shaping functional properties. Such heteromerization has also been found in the
120 CALHM family of large-pore channels, where the paralogs CALHM1 and 3 oligomerize to form
121 channels that are activated by membrane depolarization and the decrease of the extracellular Ca^{2+}-
122 concentration (Ma et al., 2018b). To probe whether this property would also extend to other family
123 members, we have initially investigated the ability of the three placental paralogs CALHM2, 4 and
124 6 to form heteromeric assemblies. To this end, we have co-transfected HEK293 cells with pairs of
125 constructs coding for different paralogs and containing unique tags for affinity purification. After
126 solubilization, specific subunits were captured via their attached tags and the sample was assayed
127 for the co-purification of the second subunit by SDS-PAGE and Western blot. In that way, we
128 have identified robust heteromerization of the paralogs CALHM2 and 4, and weak pairing of both
129 paralogs with CALHM6, thus suggesting that specific heteromerization might be a property that
130 is inherent to certain CALHM paralogs (Figure 1A).

131 After identifying the heteromerization of CALHM2 and 4, we have tested whether this process has
132 altered the activation properties of these channels. To this end we have expressed either single or
133 pairs of different CALHM paralogs in HEK293 cells and investigated their functional properties
134 by patch-clamp electrophysiology. When recorded in the whole-cell configuration, we were able
135 to reproduce the previously observed phenotype of CALHM1 to form channels that activate at
136 positive voltages (Figure 1B, Figure 1-figure supplement 1A). The observed functional properties
137 are enhanced upon co-expression of CALHM1 and 3 subunits, which results in the increase of

138 currents and activation kinetics compared to CALHM1, when recorded in the same manner (Figure
139 1C, Figure 1-figure supplement 1B). In contrast, neither CALHM2 nor CALHM4 show
140 appreciable currents under equivalent conditions, which conforms with a previous investigation
141 performed in *X. laevis* oocytes (Drozdzyk et al., 2020) (Figure 1D, Figure 1-figure supplement
142 1C). Finally, we have investigated whether their assembly as heteromers would enhance the
143 activity of CALHM2 and CALHM4 and thus proceeded with the functional characterization of
144 cells that were co-transfected with plasmids encoding each subunit. However, similar to the
145 respective homomers, we were unable to detect any current response at positive voltage, thus
146 emphasizing that these proteins share an activation mechanism that is distinct from CALHM1/3
147 (Figure 1E, F, Figure 1-figure supplement 1D, E).
148

149 **Selection of paralog-specific binders**

150 Following, we set out to characterize the structural properties of CALHM2/4 heteromers by cryo-
151 EM. This task is complicated by the unknown arrangement of subunits sharing similar structural
152 features and the potentially large compositional heterogeneity of heteromers, which might prohibit
153 classification and alignment of oligomeric complexes. We have thus initially engaged in the
154 generation of paralog-specific binders that can be used as fiducial markers to aid the identification
155 of subunits in heteromeric channels. As in previous projects, we have decided for synthetic
156 nanobodies (termed sybodies), which were selected from large construct libraries by different
157 display methods (Zimmermann et al., 2020). In independent efforts, we have selected binders
158 against homomeric assemblies of CALHM2 and CALHM4 (Figure 2-figure supplement 1) and
159 subsequently used them for a structural characterization of respective homomers to define their
160 binding epitopes and their effect on subunit conformations.

161

162 **Features of the CALHM4/SbC4 complex**

163 Our selection against CALHM4 was carried out with paired assemblies of channels containing
164 either ten or eleven subunits each, which is reflected in the low elution volume of the sample during
165 size exclusion chromatography (Figure 2-figure supplement 1B). Dimerization in CALHM4
166 proceeds at its intracellular region, resulting in large particles, which expose their extracellular
167 parts at both ends of a tubular assembly (Drozdzyk et al., 2020). This sample has allowed us to
168 isolate a specific binder, termed Sb^{CALHM4} or short SbC4, that forms a tight complex with the
169 CALHM4 channel pair, which remains intact during size exclusion chromatography as confirmed
170 by SDSPAGE (Figure 2-figure supplement 1A, B). Upon characterization by surface plasmon
171 resonance, we measured a binding affinity of about 100 nM (Figure 2-figure supplement 1C).
172 Conversely, we did not find any evidence of this protein to engage in strong interactions with
173 CALHM2 (Figure 2-figure supplement 1D). When investigated by cryo-EM, we observed two
174 populations of particles either exhibiting D10 or D11 symmetry (corresponding to dimers of
175 decameric and undecameric channels) that closely resemble equivalent structures of CALHM4
176 determined in previous studies (Drozdzyk et al., 2020) (Figure 2-figure supplement 2). Between
177 the two populations, the reconstruction of the density with D10 symmetry imposed was of higher
178 resolution and we thus restrict our detailed analysis to this structure (Figure 2A, B, Figure 2-figure
179 supplement 2). Subunits in the oligomeric assembly are arranged around an axis of symmetry,
180 which presumably defines the pore of a large channel (Figure 2B). Each subunit contains four
181 membrane-spanning helices, three of which (TM2-4) are tightly interacting to form an outer ring
182 with large diameter that separates the inside of the pore from its surrounding membrane
183 environment (Figure 2C, D). In this ring, TM2 and 4 of adjacent subunits engage in extended

184 interactions (Figure 2D). In contrast, TM1 forms an inner ring of helices lining the pore, with the
185 bent helical N-terminus (NH) running perpendicular to the membrane and projecting towards the
186 pore axis (Figure 2D). TM1 packs against TM3 of the outer ring but is not involved in direct
187 subunit interactions. Within each channel, we find residual density of low resolution, whose
188 distribution resembles the headgroup region of a lipid bilayer, which was thus previously ascribed
189 to a membrane assembled in the lumen of the pore (Drozdzyk et al., 2020) (Figure 2E). In this
190 cryo-EM map, we find density of sybodies binding at the extracellular side of each subunit forming
191 two rings of binders at both ends of the assembly (Figure 2A, B). Although not sufficiently well
192 resolved to define detailed interactions with certainty, neighboring sybodies appear not to clash
193 with epitopes being confined to a single subunit, which provides ideal properties for the
194 identification of CALHM4 subunits in heteromeric channels.
195

196 **Features of the CALHM2/SbC2 complex**

197 In case of CALHM2, our selection efforts have allowed us to identify a binder termed Sb^{CALHM2}
198 (short SbC2) forming tight complexes with homomeric assemblies (Figure 2-figure supplement
199 1A, E-G). This sybody remains bound to the channel during size exclusion chromatography, which
200 is manifested in the decreased elution volume of the complex and the presence of both proteins in
201 peak fractions as confirmed by SDS-PAGE (Figure 2-figure supplement 1E). As in case of SbC4,
202 the binding is subunit specific (Figure 2-figure supplement 1F, G). We have then proceeded with
203 the structural characterization of CALHM2/SbC2 complexes by cryo-EM and found two
204 populations of particles showing either C10 or C11 symmetry. In this data-set, only the
205 reconstruction of undecameric particles resulted in high resolution density that resembles
206 structures of CALHM2 determined in previous studies (Choi et al., 2019; Demura et al., 2020;

207 Syrjanen et al., 2020) (Figure 3A, B, Figure 3-figure supplement 1). In contrast to the CALHM4
208 structure, we did not detect any dimerization of channels (Figure 3-figure supplement 1). Another
209 pronounced difference of the CALHM2 structure concerns the conformation of TM1, which is
210 detached from its interaction with TM3 as found in CALHM4 and instead projects towards the
211 pore axis (Figure 3C). Due to its high mobility, the density of this helix is only defined at its C-
212 terminal end at the boundary to the extracellular loop connecting to TM2, whereas its remainder
213 towards the N-terminus is not resolved (Figure 3C). This arrangement of TM1 in an 'up' position
214 resembles the conformation observed in a previous structure of a complex of CALHM2 with its
215 putative inhibitor rubidium red, although its density in the inhibitor complex is better defined (Choi
216 et al., 2019). In contrast to CALHM4, where TM3 and TM4 of the same subunit tightly interact
217 throughout, in CALHM2 both helices have moved apart at their intracellular halve (Figure 3D). In
218 the structure, the resulting narrow fenestration connecting the channel interior and the membrane
219 is filled by a bound lipid (Figure 3D). Finally, unlike in the CALHM4 structure where TM1 resides
220 in a 'down' conformation, the lumen of the CALHM2 channel does not contain pronounced
221 bilayer-like residual density (Figure 3E). In the CALHM2 assembly, strong density of appropriate
222 size and shape at each of the subunits defines the location of SbC2 binding to the intracellular side
223 of the channel via its extended CDR3 loop (Figure 3A-E). On CALHM2, the epitope encompasses
224 residues located on the intracellular end of TM3, the region immediately following TM4 and part
225 of the C-terminal loop connecting the short helices CT2H and CT3H of the contacted subunit.
226 Additionally, the very C-terminus of the adjacent subunit (CT^{+1}, located in counterclockwise
227 position when viewed from the extracellular side), which contains six additional residues added to
228 the expression construct contributes to the interaction (Figure 3D). This C-terminus is unstructured
229 in absence of the sybody but contacts the region preceding CT3H on the neighboring CALHM2

230 subunit and the CDR3 region of SbC2 to become partly buried in the binding interface (Figure
231 3D). As a consequence, about 75% of the binding interface covering about 2'200 $Å^2$ of the
232 combined molecular surface is contributed by the CT^{+1}. Despite the described involvement of CT^{+1}
233 to SbC2 binding, sybodies bound to neighboring subunits do not overlap and bind remote from the
234 primary subunit interface and thus clearly label CALHM2 subunits engaging in homomeric
235 interactions in the +1 position.
236

237 **Characterization of CALHM2/4 heteromers**

238 Their high selectivity combined with the distinct location of their epitopes make the two sybodies
239 complementary tools for the identification of paralogs in heteromeric channels. We have thus used
240 both binders for the structure determination of channels consisting of CALHM2 and CALHM4
241 subunits (CALHM2/4). To this end, we have transfected HEK-293 cells with equimolar amounts
242 of DNA encoding constructs of the respective paralogs and isolated heteromeric channels by
243 tandem purification, sequentially capturing the different tags that are attached to either construct.
244 This strategy has allowed us to isolate channels containing both subunits, which constitute a small
245 fraction (<10%) of the total expressed protein, most of which assembles as homomers. We have
246 then added sybodies in stoichiometric excess and determined two datasets of CALHM2/4-sybody
247 complexes, one containing both binders and a second SbC4 only. Both datasets are of high quality
248 and provide insight into the organization of heteromeric channels with the sybodies defining the
249 distribution of CALHM2 and 4 subunits (Figure 4-figure supplements 1 and 2). In both datasets,
250 the position of CALHM4 subunits is marked by the binding of SbC4 to the extracellular part of
251 the protein, whereas the dataset containing both sybodies, SbC2 additionally labels CALHM2
252 subunits. Both samples show a heterogeneous distribution of complexes with variable ratio of the

253 two paralogs, which in all cases segregate into clusters to minimize heteromeric interactions
254 (Figure 4-figure supplements 1 and 2). A 3D classification shows particles of three distinct
255 oligomeric organizations. A population of proteins with D10 symmetry exhibits the characteristic
256 organization of CALHM4 channels, which pairwise interact on their intracellular side (Figure 4A,
257 Figure 4-figure supplement 2B). These channels consist predominantly of CALHM4 with
258 interspersed CALHM2 subunits (Figure 4A). In contrast, in two larger populations of undecameric
259 and dodecameric channels that do not dimerize, CALHM2 subunits predominate (Figure 4B, C).
260 A further classification resulted in a distribution of channels containing two to four consecutively
261 arranged CALHM4 subunits, thus suggesting that tight homotypic interactions between subunits
262 prevail in heteromeric channels (Figure 4B, C).
263

264 **Features of heteromeric CALHM2/4 channels**

265 Although our 3D classification has defined a broad distribution of different heteromeric assemblies
266 of CALHM2/4 channels, the population in each distinct assembly is too small to reach high
267 resolution. We have thus pooled the classes of all undecameric channels containing 2-4 copies of
268 CALHM4, and proceeded with further map refinement, which has allowed us to obtain maps
269 extending to global resolutions of 3.8 Å and 3.3 Å for the datasets of samples containing either
270 SbC4 only (CALHM2/4/SbC4), or both SbC4 and SbC2 (CALHM2/4/SbC2/SbC4), respectively
271 (Figure 5, Figure 4-figure supplements 1 and 2). The two cryo-EM densities provide congruent
272 views of the relative arrangement and conformational preferences of CALHM2 and 4 subunits in
273 heteromeric channels. In both datasets, the two positions uniformly occupied by CALHM4
274 (referred to as 1 and 2 when numbered in counterclockwise direction from the extracellular side)
275 are well defined and clearly discernable by SbC4 bound to its extracellular epitope (Figure 5).

276 Similarly, the seven following positions (3-9), occupied by CALHM2, are well defined, whereas
277 the two positions adjacent to the two CALHM4 subunits in clockwise direction (11 and 10), which
278 contain CALHM2 or 4 at different ratios are of somewhat lower resolution due to the averaging of
279 two different subunits. This feature is particularly pronounced in the dataset of
280 CALHM2/4/SbC2/SbC4, containing both sybodies, where position 11 bears closer resemblance to
281 CALHM4, as further evidenced by weak residual density of SbC4 (Fig. 5D). Conversely, features
282 in the neighboring position 10 are closer to CALHM2, as expected for an average of channel
283 populations containing two to four CALHM4 subunits (Figure 5D). In the
284 CALHM2/4/SbC2/SbC4 complex, most of the positions occupied by CALHM2 (*i.e.* positions 4-
285 8) are also distinguished by strong density of SbC2 binding to its intracellular epitope (Figure 5D).
286 However, since the C-terminus of the neighboring CALHM2 (CT^{+1}) contributes to binding, we
287 find weaker density in position 9 (Figure 5D). In contrast, the weaker density of SbC2 in position
288 3, which is fully occupied by CALHM2, is probably a consequence of the distinct conformation
289 of this particular subunit, which compromises sybody binding.
290

291 **Conformational properties of single subunits in CALHM2/4 channels**

292 Whereas in CALHM2/4 heteromers, the CALHM4 subunits reside in the preferential 'down'
293 conformation observed in homomeric channels, irrespective of their relative position in the
294 channel, the conformational properties of CALHM2 subunits are influenced by their environment
295 (Figure 6A). CALHM2 subunits that are distant from CALHM4 predominantly reside in the
296 familiar 'up' position of TM1 observed in in the structure of the CALHM2/SbC2 complex (Figure
297 6A). In contrast, CALHM2 in position 3 shows a distinct conformation, where TM1 has rearranged
298 to maximize its contacts with TM3, resembling the 'down' conformation of adjacent CALHM4

299 subunits (Figure 6A, B). As a consequence of this interaction, TM2 and TM3 have moved towards
300 the outer ring of helices constituted by TM2-4 to close the fenestration between TM3 and TM4,
301 which in the CALHM2/SbC2 complex was found to be occupied by a lipid (Figure 3D, Figure 6B,
302 C). These movements affect the local structure of the epitope recognized by SbC2 as manifested
303 in the weaker density observed in the CALHM2/4/SbC2/SbC4 complex, which indicates a
304 deterioration of the interaction (Figure 5D). The influence of CALHM4 on CALHM2
305 conformations is also observed in position 4, where we find a mix of both states, and in weak
306 density of the 'down' conformation in CALHM2 subunits located remote from CALHM4. The
307 distinct preference of subunit conformations is also manifested in the distribution of residual
308 density in the pore region, which is evident in low-pass filtered maps (Figure 6D). Here we find a
309 pronounced toroidal density surrounding subunits in a down-conformation, which contains
310 bilayer-like features observed in CALHM4 homomers and which is absent around CALHM2
311 subunits sharing a predominant up-conformation (Figures 2D, 3E and 6D). Together, our results
312 have defined the oligomeric organization of heteromeric channels composed of CALHM2 and 4
313 subunits and they show how their assembly impacts the conformational preference of subunits.
314

315 **CALHM Subunit interfaces**

316 The CALHM2/4 heteromer contains four distinct subunit interfaces that provide insight into the
317 structural basis for heteromerization. Whereas the homotypic interactions between pairs of
318 CALHM2 or CALHM4 subunits are essentially identical as in the respective homomeric channels,
319 the structure also reveals the well-defined interaction interface between CALHM4 and 2 subunits
320 (viewed from the extracellular side in counterclockwise direction) whereas the details of the 2/4
321 interface are blurred by the mix of subunits at the 10 and 11 positions (Figures 5 and 7). With

322 5,400 Å^2, the interface buried between two CALHM2 subunits is 40% larger compared to the
323 corresponding CALHM4 interface (burying 3960 Å^2), with latter being similar in size to the
324 heteromeric CALHM4/CALHM2 interface (3572 Å^2, Figure 7A-C). The larger surface buried
325 between CALHM2 subunits, which presumably translates in a stronger interaction, reflects the
326 observed prevalence of homomers upon coexpression of subunits. In CALHM2/4 heteromers it
327 accounts for the dominance of one paralog in different channel populations combined with the
328 observed segregation of subunits (Figure 4).
329 The subunit interfaces consist of two separated parts, one contributed by the membrane-inserted
330 helices TM2 and TM4, and the other by the cytoplasmic parts following TM4, comprising the
331 helix CTH and subsequent regions (Figure 7A-C). Within the membrane, contacts are similar and
332 dominated by hydrophobic residues several of which are conserved between both paralogs,
333 although polar contacts extend further to the extracellular region in CALHM2 (Figure 7A). In the
334 cytoplasmic domain, the interactions show pronounced differences with the contact area buried by
335 CALHM2 being considerably larger (3,003 Å^2) compared to CALHM4 (1,909 Å^2), which is a
336 consequence of the parts located C-terminally to CTH, which differ in both paralogs (Figure 7D,
337 E). Whereas interactions mediated by the conserved CTH are similar between CALHM2 and 4,
338 the following region in CALHM2 consists of three short helices (CTH', CT2H and CT3H), and
339 connecting loops which wrap around CTH to increase the interface and contribute to subunit
340 interactions (Figure 7D). In CALHM4, of these three short helices only CT3H is present which
341 engages in similar conserved interactions with the CTH as the equivalent region in CALHM2,
342 although with different subunits (Figure 7E). While, due to the altered location of CT2H, the helix
343 in CALHM2 primarily binds to an epitope located in the interacting subunit in the +1 position, in
344 CALHM4 the helix binds to the equivalent region in the same subunit. A generally similar pattern

345 of interactions is also found between subunits at the CALHM4/2 interface where the buried surface
346 area at the C-terminus is even smaller than in CALHM4/4 interfaces (1,671 $Å^2$, Figure 7F). In
347 summary, we find conserved complementary contacts between CALHM2 and CALHM4 subunits,
348 which promote the formation of heteromeric channels. However, the larger area that is buried in
349 interfaces relating equivalent subunits underlines the observed prevalence of homomeric
350 interactions.
351

352 **Discussion**

353 The formation of heteromers of close paralogs of a protein family is a common mechanism in
354 eukaryotic ion channels to confer distinct functional properties to an oligomeric assembly.
355 Heteromeric assemblies are found in pentameric ligand-gated ion channels, glutamate receptors
356 and volume-regulated anion channels of the LRRC8 family (Baumann et al., 2001; Greger and
357 Mayer, 2019; Voss et al., 2014). In the CALHM family of large pore channels, the formation of
358 heteromers has been demonstrated for the paralogs CALHM1 and CALHM3, where the pairing of
359 subunits results in a strong improvement of the activation properties compared to their homomeric
360 equivalents (Figure 1B, C) (Ma et al., 2018b). We reasoned that a similar process might also extend
361 to other family members and thus investigated the heteromerization of three paralogs that we have
362 previously shown to be expressed in placental epithelia but for which we were so far unable to
363 detect any function (Drozdzyk et al., 2020). Our experiments here have demonstrated the ability
364 of at least two paralogs, CALHM2 and 4, to form heteromeric assemblies (Figure 1A). Although
365 the existence of such mixed assemblies in a cellular context is still uncertain, our study has shed
366 light on the detailed features of the interaction of both subunits. In that way it has revealed

367 energetic relationships between homo- and heteromeric subunit pairing, providing insight that
368 might also be relevant for other ion channels.
369 The ability to form heteromers appears specific to certain members of the CALHM family, since
370 not all of the investigated combinations of paralogs were equally suited to interact (Figure 1A).
371 The general, ability of subunits to become part of the same assembly is encoded in their structure.
372 Based on the comparison of known structures, there is an apparent incompatibility between one
373 group consisting of CALHM1 and 3 and the second encompassing CALHM 2, 4, 5, and 6. This is
374 reflected in the distinct orientation of the C-terminal domain, which constitutes a large part of the
375 interaction interface (Figure 8A, B). In its orientation, the first helix of this domain termed CTH
376 is similar in CALHM2, 4, 5 and 6 and, although different degrees of pairing have been detected
377 between these subunits (Figure 1A), the energetic penalty to form heteromers is presumably small
378 (Figure 8A). In contrast, the conformation of the C-terminus of CALHM1 and presumably also
379 CALHM3 would likely interfere with their incorporation in a heteromeric assembly with any of
380 the other four subunits (Figure 8B). In this respect it is noteworthy that the same unit was
381 previously shown to be responsible for the smaller oligomeric assembly of CALHM1 as either
382 heptamer or octamer (Ren et al., 2022; Syrjanen et al., 2020). The fact that in case of the co-
383 expression of CALHM2 and CALHM4, the homomeric populations prevail, underlines the
384 energetic preference of homotypic interactions. Such prevalence was previously also observed
385 upon overexpression of different members of the unrelated LRRC8 family (Rutz et al., 2023),
386 where homomeric assemblies are believed not to be present in a cellular environment, pointing
387 towards a tightly regulated oligomerization process that might be disturbed upon overexpression.
388 However, in contrast to LRRC8A/C heteromers which, when expressed under equivalent
389 conditions, adopt a single oligomeric organization with a 2:1 ration of A to C subunits (Rutz et al.,

390 2023), we find a broad distribution of different assemblies in case of CALHM2/4 heteromers
391 (Figures 4 and 8C). For either protein family, the predominance of one of the paralogs and a
392 segregation of subunits within the oligomer provides additional evidence for the higher affinity of
393 homomeric interactions (Figure 8C).
394 Finally, we found a similar general prevalence of subunit conformations observed in homomers
395 also in heteromeric assemblies, except that in some cases the distribution of conformations is
396 influenced by their neighborhood. This is illustrated in the preference of CALHM2 subunits to
397 reside in a lifted 'up' conformation of TM1 if the subunit is located distant from CALHM4 subunits
398 whereas this conformation changes into a 'down' conformation in vicinity to CALHM4 subunits
399 (Figure 5 and 6A). The conformational preference of subunits is also extended to the shape of
400 residual density inside the pore, which exclusively around subunits in a 'down' conformation
401 shows the described bilayer-like features found in CALHM4 channels (Figure 6D and 8D). These
402 observations underline the general independence of subunits in assuming their conformation but
403 also indicate some coupling between neighbors. Thus, a change between conformations would not
404 necessarily have to proceed as a fully concerted transition.
405
406 Despite the observed diversity of subunit assemblies and pore conformations in CALHM2/4
407 heteromers, it is puzzling not to find detectable changes in their functional properties, as neither
408 of the constructs shows any sign of activity under conditions where CALHM1/3 heteromers
409 robustly conduct ions (Figure 1B-F, Figure 1-figure supplement 1), despite the fact that their larger
410 assembly should result in a wider pore diameter. The activation properties of these CALHM
411 paralogs have thus remained elusive and might require still unidentified interaction partners.
412 Alternatively, we also cannot exclude that these large oligomers might serve a function or substrate

413 preference that differs from classical large pore channels, which could be modified by the observed
414 formation of heteromers.
415
416 **Methods**

417 **Expression constructs**

418 CALHM coding sequences (synthesized by GeneScript) were inserted into a modified FX-cloning
419 compatible pcDNA1.3 vector (Drozdzyk et al., 2020; Geertsma, 2013; Geertsma and Dutzler,
420 2011). The expressed CALHM constructs contained at their C-terminus either a Venus, myc and
421 Streptavidin-Binding Peptide (Venus-myc-SBP) tag or a myc and His_6 (myc-His) tag. A 3C
422 protease cleavage sequence between the CALHM and tag sequences permitted removal of the c-
423 terminal fusion after purification. Sybody coding sequences were cloned into the FX-compatible
424 pSb_init vector, which contains a chloramphenicol-resistance gene and an arabinose-inducible
425 promotor (Zimmermann et al., 2020). The expressed sybody constructs contained an N-terminal
426 pelB leader sequence and a C-terminal His_6-tag. To obtain tag-free sybodies used in structural
427 characterization of heteromeric CALHM2/4 channels, sybody sequences were cloned into a vector
428 containing an N-terminal pelB signal sequence followed by a His_{10}-tag, maltose binding protein
429 and a 3C cleavage site (pBXNPHM3).

430

431 **Expression in HEK 293 suspension cell culture**

432 Human CALHM proteins were transiently expressed in suspension HEK293 GnTI$^-$ cells (ATCC
433 CRL-3022) following previously described protocols (Drozdzyk et al., 2020). HEK293 GnTI$^-$

434 cells were cultured in HyCell HyClone TransFx-H medium (Cytiva) supplemented with 1% fetal
435 bovine serum (FBS), 4 mM L-glutamine, 1.5% Poloxamer 188, and penicillin/streptomycin. The
436 cells were maintained at 37 °C in a humidified incubator at a 5% CO_2 atmosphere at 185 rpm. One
437 day before transfection, the cells were diluted to a density of 5 10^5 cells/ml and transfected with a
438 mixture of DNA and PEI. In co-transfections, a mixture of DNA constructs at equivalent molar
439 ratio was used. For 300 ml of cell culture, 0.5 mg of DNA and 1.2 mg of PEI MAX were each
440 suspended in 16 ml of DMEM medium. DNA solutions were mixed with the PEI solutions and
441 incubated for 15 minutes. To increase transfection efficiency, the mixture was supplemented with
442 4 mM valproic acid. The transfection mixtures were then added to cell cultures and expression was
443 carried out for 36 hours. After this period, the cells were pelleted by centrifugation at 500 g for 25
444 min, washed with PBS buffer and stored at -20 °C for further use.

445

446 **CALHM protein purification**

447 All protein purification steps were conducted at 4 °C. HEK293 cells expressing SBP-tagged
448 CALHM proteins for purification of homomeric channels or co-expressing SBP tagged CALHM2
449 and His_{10}-tagged CALHM4 for purification of heteromeric channels were harvested (typically
450 from 1 to 2 l of cell culture for purification of homomeric channels and from 9 l for purification of
451 heteromeric channels) and suspended in lysis buffer consisting of 25 mM HEPES (pH 7.6), 150
452 mM NaCl, 1% lauryl maltose-neopentyl glycol (LMNG), 0.5 mM $CaCl_2$, 2 mM $MgCl_2$, protease
453 inhibitors, RNase and DNase. After 1 hour, the lysate was clarified by centrifugation at 15,000 g
454 for 20 min. The clarified lysate was mixed with Strep-Tactin SuperFlow resin (1 ml of bed-resin
455 per 5 g of cell pellet) and incubated for 1 hour. Following, the resin was washed with 5 column

456 volumes (CV) of SEC buffer containing 10 mM HEPES (pH 7.6), 150 mM NaCl, 50 µM GDN, 2
457 mM $CaCl_2$. Bound proteins were eluted from the resin using 3 CV of SEC buffer supplemented
458 with 10 mM d-biotin. For the isolation of heteromeric CALHM2/4 channels, an extra affinity
459 chromatography step on Ni-NTA resin was performed after the initial purification on Strep-Tactin
460 resin. To this end, the eluate from the first purification step was incubated with NiNTA resin at a
461 1:6 v/v ratio and incubated for 1 hour under gentle agitation. Subsequently, the resin was washed
462 with 30 column volumes (CV) of SEC buffer, and bound proteins were eluted using the same
463 buffer supplemented with 300 mM imidazole. To remove fusion tags, eluates were incubated with
464 a 1:1 molar ratio of 3C protease for 30 min. Samples were then concentrated to 0.5 ml using an
465 Amicon Ultra centrifugal filter (100 kDa cutoff; Millipore), filtered through 0.22 µm filters and
466 subjected to size exclusion chromatography on a Superose 6 10/300 GL column equilibrated with
467 SEC buffer. Peak fractions were pooled, concentrated using a 100 kDa MWCO centrifugal filter
468 and immediately used for the preparation of cryo-EM grids.

469

470 **Pulldown binding assays**

471 For pull-downs of CALHM homologues, HEK293 GnTI$^-$ cells were co-transfected using mixtures
472 of vectors encoding one CALHM paralog containing a fusion to Venus-myc-SBP and another
473 paralog containing a myc-His tag at equivalent molar ratios. All steps of the pulldown binding
474 assays were performed at 4 °C. Cells from a 300 ml culture were lysed in lysis buffer (25 mM
475 HEPES (pH 7.6), 150 mM NaCl, 1% LMNG, protease inhibitors, RNase, DNAse, 0.5 mM $CaCl_2$,
476 2 mM $MgCl_2$) for 1 hour and the lysates were cleared by centrifugation at 15,000 rcf for 10 min.
477 The supernatants were filtered through a 5 µm filter, mixed with 2 ml of Strep-Tactin SuperFlow

478 resin and incubated for 2 hours under gentle agitation. The resin was then washed with 5 CV of
479 wash buffer and bound proteins were eluted with elution buffer (wash buffer supplemented with
480 10 mM d-desthiobiotin, pH 7.6). For Western blot analysis, samples were loaded on a 4–20%
481 SDS-polyacrylamide gel and transferred to a polyvinylidene fluoride membrane by a semi-dry
482 blotting procedure. The membranes were first blocked at room temperature for 1 hour with 5%
483 non-fat milk in TBST buffer (50 mM Tris (pH 7.6), 150 mM NaCl, 0.075% Tween20) and then
484 incubated with anti-Myc primary antibodies overnight at 4 °C. The membranes were then washed
485 three times for 20 min with TBST and incubated with horse-radish peroxidase-conjugated goat
486 anti-mouse IgG antibody in 5% milk-TBST at room temperature for 1 hour. To remove unbound
487 primary antibodies, the membranes were washed with TBST buffer and subsequently blotted with
488 goat anti-rabbit-HRP conjugated secondary antibody for 2 hours at 4 °C. After blotting, the
489 membranes were washed with TBST buffer and developed with the Amersham ECL Prime
490 Western Blotting Detection kit (GE Healthcare).

491

492 **Sybody selection**

493 For sybody selection procedures, CALHM2 and CALHM4 proteins were chemically biotinylated
494 using amine-reactive EZ-Link™ NHS-PEG4-Biotin (ThermoFisher Scientific). For this purpose,
495 proteins were diluted to a concentration of 25 µM in SEC buffer and the coupling agent was added
496 at an 8-fold molar excess. Samples were incubated for 1 hour on ice and the reaction was quenched
497 by the addition of 5 mM Tris-HCl (pH 8.0). Excess biotin was removed from the biotinylated
498 protein on a PD-10 desalting column. The eluted proteins were concentrated, mixed with glycerol
499 to a final concentration of 10%, aliquoted, flash frozen in liquid N_2 and stored at -80 °C. Sybody

500 selection was performed as previously described (Zimmermann et al., 2020). Three synthetic
501 ribosome-display libraries, concave, loop , and convex libraries, and the plasmids, were kindly
502 provided by Prof. Markus Seeger. Sybodies were selected against chemically biotinylated
503 CALHM proteins. In brief, one round of ribosome display was performed, and the output RNA
504 was reverse transcribed and cloned into a phage-display compatible vector. The obtained plasmids
505 were transformed into *E. coli* SS320 cells to produce phages using a helper phage M13KO7. The
506 produced phages were then used in subsequent two rounds of phage display. Phagemids were
507 isolated from the output phages of the second round, and the sequences coding for sybodies were
508 subcloned into an pSB_init expression vector. The resulting plasmids were transformed into *E.*
509 *coli* MC1061, which were plated on agar plates. Single clones were expressed on a small scale and
510 used for binding tests by ELISA. Positive clones were sequenced.

511

512 **Sybody expression and purification**

513 DNA constructs of sybodies were transformed into *E. coli* MC1061 by a heat shock procedure and
514 grown in one liter of Terrific Broth medium supplemented with 25 µg/ml chloramphenicol at
515 37 °C. After initial incubation at 37 °C for 2 hours, the temperature was lowered to 22 °C and once
516 the cultures reached an OD_{600} of 0.5, L-arabinose was added to a final concentration of 0.02% to
517 induce expression. After 16-18 hours of expression, bacteria were harvested by centrifugation at
518 8,000 g for 20 min and pellets were either used immediately or stored at -80 °C until further use.
519 For purification, pellets were resuspended in TBS buffer (50 mM Tris (pH 7.6), 150 mM NaCl)
520 supplemented with 0.1 mg/ml lysozyme at a 1:30 w/v ratio. Bacteria were lysed by three freeze-
521 thaw cycles followed by sonication to release the periplasmic content. Lysates were centrifuged at

522 8,000 g for 30 min at 4 ºC. The supernatants were collected and mixed with Ni-NTA resin and
523 incubated for 30 min. The resin was washed with TBS and sybodies were eluted with TBS
524 supplemented with 300 mM imidazole. For removal of the affinity tag, eluates were incubated
525 overnight with 3C protease while dialyzing with a MWCO of 5 kDa. The eluates were then
526 concentrated and filtered through a 0.22 µm centrifugal filter and subjected to size exclusion
527 chromatography on a Sepax SRT-10C SEC100 column equilibrated in TBS. Fractions of the
528 monomeric sybody peaks were collected and stored at -80 ºC for further use.

529

530 **Binding assays**

531 Purified CALHM proteins were mixed with sybodies in a molar ratio of 1:2 to a final concentration
532 of 25 µM CALHM proteins. Prior to mixing, sybodies were supplemented with GDN to a final
533 concentration of 50 µM. Protein mixtures were applied to a Superose 6 5/150 Increase column
534 equilibrated with SEC buffer. Peak fractions corresponding to CALHM proteins were collected,
535 concentrated using Amicon Ultra 0.5 ml centrifugal filters (10 kDa cut-off, Ultracel) and analyzed
536 by SDS-PAGE. SPR measurements were performed at the Functional Genomic Centre Zurich
537 using a Biacore T200 instrument (GE Healthcare). The chemically biotinylated CALHM proteins
538 were immobilized on a streptavidin-coated sensor chip (XanTec), resulting in a maximum response
539 value of approximately 600 response units (RU). Measurements were performed at 10°C at a flow
540 rate of 30 µl/min. The buffer used during the experiments consisted of 10 mM HEPES at pH 7.6,
541 150 mM NaCl, 2 mM $CaCl_2$ and 0.006% GDN for CALHM2 or 0.01% LMNG for CALHM4.
542 Flow cell 1 was left empty to act as a reference cell for the measurements. Prior to measurements,
543 the system was equilibrated with the appropriate buffer for 2 hours. The sybodies were injected in

544 a single cycle kinetic measurement at concentrations of 7.8, 15.6, 31.25, 125 and 500 nM for
545 sybody SbC2 and 8, 24, 72, 216 and 648 nM for sybody SbC4. Binding data was analyzed using
546 BIAevaluation software (GE Healthcare) and fitted to a single-site binding model.

547

548 **Whole-cell patch-clamp recordings**

549 Adherent HEK293T cells were gently detached from their support and seeded in 10-cm dishes at
550 10% confluency. After a 3-hour incubation, cells were transfected with a mixture of 12 µg PEI and
551 3 µg of plasmids encoding CALHM constructs, which were C-terminally tagged with Venus-Myc-
552 SBP. For co-expression experiments, cells were transfected at a 1:1 ratio of the constructs at a total
553 amount of 3 µg of plasmids. Mock cells were transfected with a vector expressing Venus tag only.
554 Prior to transfection, DNA and PEI were separately incubated in 0.5 ml of DMEM medium. After
555 5 min, both solutions were mixed, incubated for 15 min and added to respective cell cultures.
556 Whole-cell currents were recorded 16-24 hours after transfection at room temperature (20-22 °C).
557 Recordings were conducted using borosilicate glass capillaries that were pulled and polished to
558 achieve a final resistance of 4-6 MΩ. Patches were held at -40 mV and the voltage was altered
559 between -100 mV and +100 mV in 10 mV increments for 500 ms by a step protocol. Cells were
560 perfused using a gravity-fed system. The solutions were as previously described (Syrjanen et al.,
561 2020). The pipette solution contained 147 mM NaCl, 10 mM EGTA, and 10 mM HEPES at pH
562 7.0, using NaOH for adjusting the pH. The bath solution contained 147 mM NaCl, 13 mM glucose,
563 10 mM HEPES (pH 7.3), using NaOH for adjusting the pH, 2 mM KCl, 2 mM $CaCl_2$, and 1 mM
564 $MgCl_2$. In Ca^{2+}-free experiments, the bath solution was similar but without addition of $CaCl_2$. Data
565 acquisition was performed using an Axopatch 200B amplifier and either Digidata 1440 or 1550

566 (Molecular Devices). Analog signals were digitized at a sampling rate of 10-20 kHz and filtered
567 at 5 kHz using the built-in 4-pole Bessel filter. Clampex 10.6 software (Molecular Devices) was
568 used for data acquisition and GraphPad Prism 8 for data analysis.
569
570 **Cryo-EM sample preparation and data collection**

571 Cryo-EM grids were prepared with freshly purified CALHM proteins. Prior to freezing, sybodies
572 were added to the CALHM samples at a 1:1.5 molar excess (based on the total amount of CALHM
573 subunits). In the sample containing heteromeric CALHM2/4 channels and both sybodies, SbC4
574 was added at a 1.5 and SbC2 at a 2.5 molar excess. The samples were frozen at different
575 concentrations of CALHM proteins (20 µM in the CALHM2/SbC2 sample, 47 µM in the
576 CALHM4/SbC4 sample, 38 µM in the CALHM2/4/SbC4 sample and 45 µM in the
577 CALHM2/4/SbC2/SbC4 sample). Samples were applied to glow-discharged holey carbon grids
578 (Quantifoil R1.2/1.3 Au 200 mesh). Excess liquid was removed in a controlled environment (4 °C
579 and 100% relative humidity) by blotting grids for 2–4 s. Grids were subsequently flash-frozen in
580 a liquid propane-ethane mix using a Vitrobot Mark IV (Thermo Fisher Scientific) and stored in
581 liquid nitrogen. Samples were imaged with a 300 kV Titan Krios G3i with a 100 µm objective
582 aperture and data were collected using a post-column BioQuantum energy filter with a 20 eV slit
583 and a K3 direct electron detector operating in super-resolution counted mode. Dose-fractionated
584 micrographs were recorded with a defocus range of -1 µm to -2.4 µm in an automated mode using
585 EPU 2.9. Datasets were recorded at a nominal magnification of 130,000 corresponding to a pixel
586 size of 0.651 Å per pixel (0.3255 Å per pixel in super-resolution mode).

587

588 **Cryo-EM image processing**

589 Micrographs from all datasets were pre-processed in a similar manner. Micrographs of the
590 CALHM2-/SbC2, CALHM2/4/SbC4 and CALHM2/4/SbC2/SbC4 datasets were binned prior to
591 processing resulting in a pixel size of 0.651Å. The raw movies were used to correct for beam-
592 induced motion using patch motion correction in cryoSPARC v.3.2.0 and v.4.0.3, followed by
593 patch CTF estimation (Punjani et al., 2017). For the CALHM4/SbC4 dataset the raw movies were
594 used for correction of the beam-induced movement using a dose-weighting scheme in RELION's
595 own implementation of the MotionCor2 algorithm available in version 3.0 (Zivanov et al., 2018)
596 and the CTF parameters were estimated on summed movie frames using CTFFIND4.1 (Rohou and
597 Grigorieff, 2015). Poor quality images with significant drift, ice contamination or poor CTF
598 estimates were discarded.

599 The dataset of CALHM4/SbC4 was processed entirely in RELION-3.1 (Scheres, 2012). Particles
600 were first selected by Laplacian-of-Gaussian based auto-picking and subjected to a first round of
601 2D classification to generate 2D average templates. Next, four 2D classes with protein-like features
602 were used as references for a second template-based picking. The particles were extracted with a
603 box size of 720 pixels and downscaled four times. A second 2D classification was performed and
604 the particles from the five best classes were used for the generation of an initial 3D model,
605 imposing C10 symmetry. The extracted particles from the second 2D classification round were
606 subjected to a round of 3D classification with C10 symmetry imposed, using the initial model low
607 pass filtered to 60 Å as a reference map. The best 3D class was selected and the particles belonging
608 to this class were unbinned to their original pixel size and subjected to 3D refinement with D10
609 symmetry imposed. Additionally, CTF and aberration refinement and Bayesian polishing was
610 applied (Rohou and Grigorieff, 2015; Zivanov et al., 2019). The map was sharpened with an

611 isotropic b-factor of -153 $Å^2$, resulting in a global resolution of 3.7 Å. The local resolution was
612 estimated using RELION (Zivanov et al., 2018).
613 The dataset of CALHM2/SbC2 was processed entirely in cryoSPARC v.3.2.0 and v.4.0.3 (Punjani
614 et al., 2017). Particles were initially picked with the blob picker and subjected to 2D classification
615 to generate 2D average templates for more accurate template-based particle picking. Particles were
616 selected and extracted with a box size of 512 pixels and downscaled twice. Selected particles were
617 subjected to four rounds of 2D classification to remove false positives and low-quality particles
618 and subjected to an *ab initio* reconstruction with three classes. The obtained classes included
619 decameric, undecameric and ambiguous assemblies of CALHM2. Particles belonging to classes
620 showing an undecameric assembly were further sorted by a round of heterogeneous refinement
621 using three *ab initio* reconstructions as references. The same procedure was used for particles
622 belonging to classes showing a decameric assembly, which yielded a low-quality reconstruction.
623 Therefore, further processing was restricted to the more promising undecameric assemblies. The
624 quality of the reconstruction was further improved by CTF global and local refinements and non-
625 uniform refinement with C11 symmetry imposed, yielding a map at 3.07 Å. The local resolution
626 was estimated with cryoSPARC. To improve the resolution of the CALHM-sybody interface
627 region, a local refinement with C11 symmetry imposed was performed in the presence of a tight
628 mask restricted to the region surrounding the sybody binding site, yielding a reconstruction of this
629 region at a global resolution of 2.8 Å.
630 The datasets of CALHM2/4 in complex with sybodies were processed in cryoSPARC v.4.0.3
631 (Punjani et al., 2017), unless indicated otherwise. Particles from the CALHM2/4 datasets
632 containing either both sybodies (CALHM2/4/SbC2/SbC4) or SbC4 alone (CALHM2/4/SbC4)
633 were initially picked with the blob picker and subjected to 2D classification to generate 2D

634 templates for more accurate template-based particle picking. Particles were selected and extracted
635 with a box size of 512 pixels, downscaled twice and subjected to multiple rounds of 2D
636 classification to remove false positives and poor-quality particles. Visual inspection of the 2D
637 classes indicated the presence of different assemblies. To separate these assemblies, particles were
638 exported to RELION (version 4.0) (Kimanius et al., 2021) and used to generate initial models.
639 Subsequently, particles were subjected to several rounds of 3D classification using the initial
640 models as references. In the first two rounds of classification, low quality particles were excluded
641 and only particles belonging to the high-quality classes were subjected to a final 3D classification
642 with 10 distinct classes. To obtain high resolution reconstructions of complexes, particles
643 belonging to 2D classes of channel dimers were excluded and only particles belonging to high
644 quality 2D classes with single channels were used to generate *ab initio* reconstructions in
645 cryoSPARC. This yielded decoy reconstructions and undecameric reconstructions. Particles of
646 undecameric reconstructions were used as input for heterogeneous refinements with three
647 references including a decoy class and two proper classes. This approach yielded reconstructions
648 of undecameric and dodecameric assemblies. The heterogeneous refinement was repeated four
649 times using particles belonging to the undecameric assembly from the previous refinement as input
650 and undecameric and dodecameric reconstructions as references. Resulting undecameric
651 reconstructions were further improved by local and global CTF, and non-uniform refinements in
652 C1. . These approaches yielded maps with global resolutions of 3.8Å and 3.3Å for the
653 CALHM2/4/SbC4 and CALHM2/4/SbC2/SbC4 complexes, respectively. The local resolution of
654 maps was estimated within cryoSPARC.
655
656 **Model building and Refinement**

657 Models were based on previously determined structures of CALHM2 (PDB:6UIW) (Choi et al.,
658 2019) and CALHM4 (PDB:6YTL) (Drozdzyk et al., 2020). Sybodies were initially modelled
659 based on high-resolution structures (PDB:1ZVH for SbC2 and PDB:3K1K for SbC4). Models
660 were first fitted into their corresponding densities using ChimeraX (Pettersen et al., 2021). The
661 cryo-EM density of CALHM2/SbC2 allowed us to assign residues 39-308 and 314-323 of
662 CALHM2 and 324-329 of the remaining sequence of the expression tag, and the entire model of
663 SbC2 whose CDRs interacting with CALHM2 were rebuilt into the cryo-EM density. The cryo-
664 EM density of CALHM4/SbC4 was of sufficiently high resolution to unambiguously assign
665 residues 5–82 and 94–276 of CALHM4. In contrast, the limited quality of the density of SbC4 did
666 not permit a complete interpretation of its atomic model and thus a truncated version lacking the
667 variable regions was placed into the density.
668 The model of the heteromeric CALHM2/4 in complex with sybodies SbC2 and SbC4 was built by
669 placing eight CALHM2 and three CALHM4 subunits into the cryo-EM density obtained from the
670 CALHM2/4/SbC2/SbC4 dataset at 3.3 Å. Coordinates of CALHM subunits and sybodies were
671 obtained from the structures of the homomeric CALHM2/SbC2 and CALHM4/SbC4 complexes.
672 Residues 19-46 of CALHM2 in the downward conformation were built de novo. The subunit
673 displaying a mix of CALHM2 and 4 (i.e. position 10) was interpreted by a CALHM2 subunit
674 where loop regions not defined in the density were removed. The structure of the
675 CALHM2/4/SbC4 complex at 3.8 Å was built based on the model of CALHM2/4/SbC2/SbC4 after
676 removal of the SbC2 subunits, except that it contains a truncated version of CALHM2 also in
677 position 11. Refinement and validation of all models was performed in PHENIX (Afonine et al.,
678 2018). Figures containing molecular structures and densities were prepared with DINO

679 (http://www.dino3d.org), PyMOL (DeLano, 2002) and ChimeraX (Pettersen et al., 2021).
680 Interaction interfaces were calculated with CNS_SOLVE (Brunger, 2007).
681
682 **Acknowledgments** This research was supported by a grant from the Swiss National Science
683 Foundation (No. 310030B_182828). Cryo-EM data was collected at the Center for Microscopy
684 and Image Analysis (ZMB) of the University of Zurich. We thank Markus Seeger for providing
685 access to the sybody libraries. Jens Sobek and Marton Liciczai are acknowledged for help with
686 surface plasmon resonance experiments recorded at the Functional Genomics Center of UZH/ETH
687 Zurich. All members of the Dutzler lab are acknowledged for their help at various stages of the
688 project.
689
690 **Competing interests**
691 The authors declare no competing interests.
692
693 **Accession codes**
694 The cryo-EM density maps have been deposited in the Electron Microscopy Data Bank under
695 following ID codes: EMD-19365 (CALHM4/SbC4), EMD-19362 (CALHM2/SbC2), EMD-
696 19363 (CALHM2/CALHM4/SbC4), EMD-19364 (CALHM2/CALHM4/SbC2/SbC4). The
697 coordinates of the corresponding atomic models of have been deposited in the Protein Data Bank
698 under ID codes 8RMN (CALHM4/SbC4), 8RMK (CALHM2/SbC2), 8RML
699 (CALHM2/CALHM4/SbC4), 8RMM (CALHM2/CALHM4/SbC2/SbC4).
700

701 **References**

702

703 Afonine, P.V., B.K. Poon, R.J. Read, O.V. Sobolev, T.C. Terwilliger, A. Urzhumtsev, and P.D.
704 Adams. 2018. Real-space refinement in PHENIX for cryo-EM and crystallography. *Acta*
705 *Crystallogr D Struct Biol*. 74:531-544.

706 Baumann, S.W., R. Baur, and E. Sigel. 2001. Subunit arrangement of gamma-aminobutyric acid
707 type A receptors. *J Biol Chem*. 276:36275-36280.

708 Brunger, A.T. 2007. Version 1.2 of the Crystallography and NMR system. *Nat Protoc*. 2:2728-
709 2733.

710 Choi, W., N. Clemente, W. Sun, J. Du, and W. Lu. 2019. The structures and gating mechanism of
711 human calcium homeostasis modulator 2. *Nature*. 576:163-167.

712 Danielli, S., Z. Ma, E. Pantazi, A. Kumar, B. Demarco, F.A. Fischer, U. Paudel, J. Weissenrieder,
713 R.J. Lee, S. Joyce, J.K. Foskett, and J.S. Bezbradica. 2023. The ion channel CALHM6
714 controls bacterial infection-induced cellular cross-talk at the immunological synapse.
715 *EMBO J*. 42:e111450.

716 DeLano, W.L. 2002. Pymol: An open-source molecular graphics tool. *CCP4 Newsletter On*
717 *Protein Crystallography*. 40:82-92.

718 Demura, K., T. Kusakizako, W. Shihoya, M. Hiraizumi, K. Nomura, H. Shimada, K. Yamashita,
719 T. Nishizawa, A. Taruno, and O. Nureki. 2020. Cryo-EM structures of calcium homeostasis
720 modulator channels in diverse oligomeric assemblies. *Sci Adv*. 6:eaba8105.

721 Drozdzyk, K., M. Sawicka, M.I. Bahamonde-Santos, Z. Jonas, D. Deneka, C. Albrecht, and R.
722 Dutzler. 2020. Cryo-EM structures and functional properties of CALHM channels of the
723 human placenta. *Elife*. 9.

724 Foskett, J.K. 2020. Structures of CALHM channels revealed. *Nat Struct Mol Biol*. 27:227-228.

725 Geertsma, E.R. 2013. FX cloning: a versatile high-throughput cloning system for characterization
726 of enzyme variants. *Methods Mol Biol*. 978:133-148.
727 Geertsma, E.R., and R. Dutzler. 2011. A versatile and efficient high-throughput cloning tool for
728 structural biology. *Biochemistry*. 50:3272-3278.
729 Greger, I.H., and M.L. Mayer. 2019. Structural biology of glutamate receptor ion channels:
730 towards an understanding of mechanism. *Curr Opin Struct Biol*. 57:185-195.
731 Kimanius, D., L. Dong, G. Sharov, T. Nakane, and S.H.W. Scheres. 2021. New tools for automated
732 cryo-EM single-particle analysis in RELION-4.0. *Biochemical Journal*. 478:4169-4185.
733 Liao, Y., Y. Wang, Q.-Q. Tao, C. Yang, J. Wang, J. Cheng, J. Ma, Z.-Y. Wu, R.-Y. Pan, and Z.
734 Yuan. 2023. CALHM2 V136G polymorphism reduces astrocytic ATP release and is
735 associated with depressive symptoms and Alzheimer's disease risk. *Alzheimer's &*
736 *Dementia*. 19:4407-4420.
737 Liu, J., F. Wan, Q. Jin, X. Li, E.A. Bhat, J. Guo, M. Lei, F. Guan, J. Wu, and S. Ye. 2020. Cryo-
738 EM structures of human calcium homeostasis modulator 5. *Cell Discov*. 6:81.
739 Ma, J., X. Qi, C. Yang, R. Pan, S. Wang, J. Wu, L. Huang, H. Chen, J. Cheng, R. Wu, Y. Liao, L.
740 Mao, F.C. Wang, Z. Wu, J.X. An, Y. Wang, X. Zhang, C. Zhang, and Z. Yuan. 2018a.
741 Calhm2 governs astrocytic ATP releasing in the development of depression-like behaviors.
742 *Mol Psychiatry*. 23:883-891.
743 Ma, Z., A.P. Siebert, K.H. Cheung, R.J. Lee, B. Johnson, A.S. Cohen, V. Vingtdeux, P.
744 Marambaud, and J.K. Foskett. 2012. Calcium homeostasis modulator 1 (CALHM1) is the
745 pore-forming subunit of an ion channel that mediates extracellular Ca2+ regulation of
746 neuronal excitability. *Proc Natl Acad Sci U S A*. 109:E1963-1971.

747 Ma, Z., J.E. Tanis, A. Taruno, and J.K. Foskett. 2016. Calcium homeostasis modulator (CALHM)
748 ion channels. *Pflugers Arch*. 468:395-403.
749 Ma, Z., A. Taruno, M. Ohmoto, M. Jyotaki, J.C. Lim, H. Miyazaki, N. Niisato, Y. Marunaka, R.J.
750 Lee, H. Hoff, R. Payne, A. Demuro, I. Parker, C.H. Mitchell, J. Henao-Mejia, J.E. Tanis,
751 I. Matsumoto, M.G. Tordoff, and J.K. Foskett. 2018b. CALHM3 Is Essential for Rapid Ion
752 Channel-Mediated Purinergic Neurotransmission of GPCR-Mediated Tastes. *Neuron*.
753 98:547-561 e510.
754 Pettersen, E.F., T.D. Goddard, C.C. Huang, E.C. Meng, G.S. Couch, T.I. Croll, J.H. Morris, and
755 T.E. Ferrin. 2021. UCSF ChimeraX: Structure visualization for researchers, educators, and
756 developers. *Protein Science*. 30:70-82.
757 Punjani, A., J.L. Rubinstein, D.J. Fleet, and M.A. Brubaker. 2017. cryoSPARC: algorithms for
758 rapid unsupervised cryo-EM structure determination. *Nature Methods*. 14:290-296.
759 Ren, Y., Y. Li, Y. Wang, T. Wen, X. Lu, S. Chang, X. Zhang, Y. Shen, and X. Yang. 2022. Cryo-
760 EM structure of the heptameric calcium homeostasis modulator 1 channel. *J Biol Chem*.
761 298:101838.
762 Ren, Y., T. Wen, Z. Xi, S. Li, J. Lu, X. Zhang, X. Yang, and Y. Shen. 2020. Cryo-EM structure
763 of the calcium homeostasis modulator 1 channel. *Sci Adv*. 6:eaba8161.
764 Rohou, A., and N. Grigorieff. 2015. CTFFIND4: Fast and accurate defocus estimation from
765 electron micrographs. *Journal of structural biology*. 192:216-221.
766 Rutz, S., D. Deneka, A. Dittmann, M. Sawicka, and R. Dutzler. 2023. Structure of a volume-
767 regulated heteromeric LRRC8A/C channel. *Nat Struct Mol Biol*. 30:52-61.
768 Scheres, S.H. 2012. RELION: implementation of a Bayesian approach to cryo-EM structure
769 determination. *Journal of structural biology*. 180:519-530.

770 Siebert, A.P., Z. Ma, J.D. Grevet, A. Demuro, I. Parker, and J.K. Foskett. 2013. Structural and
771 functional similarities of calcium homeostasis modulator 1 (CALHM1) ion channel with
772 connexins, pannexins, and innexins. *J Biol Chem*. 288:6140-6153.
773 Syrjanen, J., K. Michalski, T. Kawate, and H. Furukawa. 2021. On the molecular nature of large-
774 pore channels. *J Mol Biol*. 433:166994.
775 Syrjänen, J.L., M. Epstein, R. Gómez, and H. Furukawa. 2023. Structure of human CALHM1
776 reveals key locations for channel regulation and blockade by ruthenium red. *Nature*
777 *Communications*. 14:3821.
778 Syrjanen, J.L., K. Michalski, T.H. Chou, T. Grant, S. Rao, N. Simorowski, S.J. Tucker, N.
779 Grigorieff, and H. Furukawa. 2020. Structure and assembly of calcium homeostasis
780 modulator proteins. *Nat Struct Mol Biol*.
781 Taruno, A., I. Matsumoto, Z. Ma, P. Marambaud, and J.K. Foskett. 2013a. How do taste cells
782 lacking synapses mediate neurotransmission? CALHM1, a voltage-gated ATP channel.
783 *Bioessays*. 35:1111-1118.
784 Taruno, A., V. Vingtdeux, M. Ohmoto, Z. Ma, G. Dvoryanchikov, A. Li, L. Adrien, H. Zhao, S.
785 Leung, M. Abernethy, J. Koppel, P. Davies, M.M. Civan, N. Chaudhari, I. Matsumoto, G.
786 Hellekant, M.G. Tordoff, P. Marambaud, and J.K. Foskett. 2013b. CALHM1 ion channel
787 mediates purinergic neurotransmission of sweet, bitter and umami tastes. *Nature*. 495:223-
788 226.
789 Voss, F.K., F. Ullrich, J. Munch, K. Lazarow, D. Lutter, N. Mah, M.A. Andrade-Navarro, J.P. von
790 Kries, T. Stauber, and T.J. Jentsch. 2014. Identification of LRRC8 heteromers as an
791 essential component of the volume-regulated anion channel VRAC. *Science*. 344:634-638.

792 Yang, W., Y. Wang, J. Guo, L. He, Y. Zhou, H. Zheng, Z. Liu, P. Zhu, and X.C. Zhang. 2020.
793 Cryo-electron microscopy structure of CLHM1 ion channel from Caenorhabditis elegans.
794 *Protein Science*. 29:1803-1815.
795 Zimmermann, I., P. Egloff, C.A.J. Hutter, B.T. Kuhn, P. Brauer, S. Newstead, R.J.P. Dawson, E.R.
796 Geertsma, and M.A. Seeger. 2020. Generation of synthetic nanobodies against delicate
797 proteins. *Nat Protoc*. 15:1707-1741.
798 Zivanov, J., T. Nakane, B.O. Forsberg, D. Kimanius, W.J. Hagen, E. Lindahl, and S.H. Scheres.
799 2018. New tools for automated high-resolution cryo-EM structure determination in
800 RELION-3. *Elife*. 7.
801 Zivanov, J., T. Nakane, and S.H.W. Scheres. 2019. A Bayesian approach to beam-induced motion
802 correction in cryo-EM single-particle analysis. *IUCrJ*. 6:5-17.

803 **Figures and figure legends**

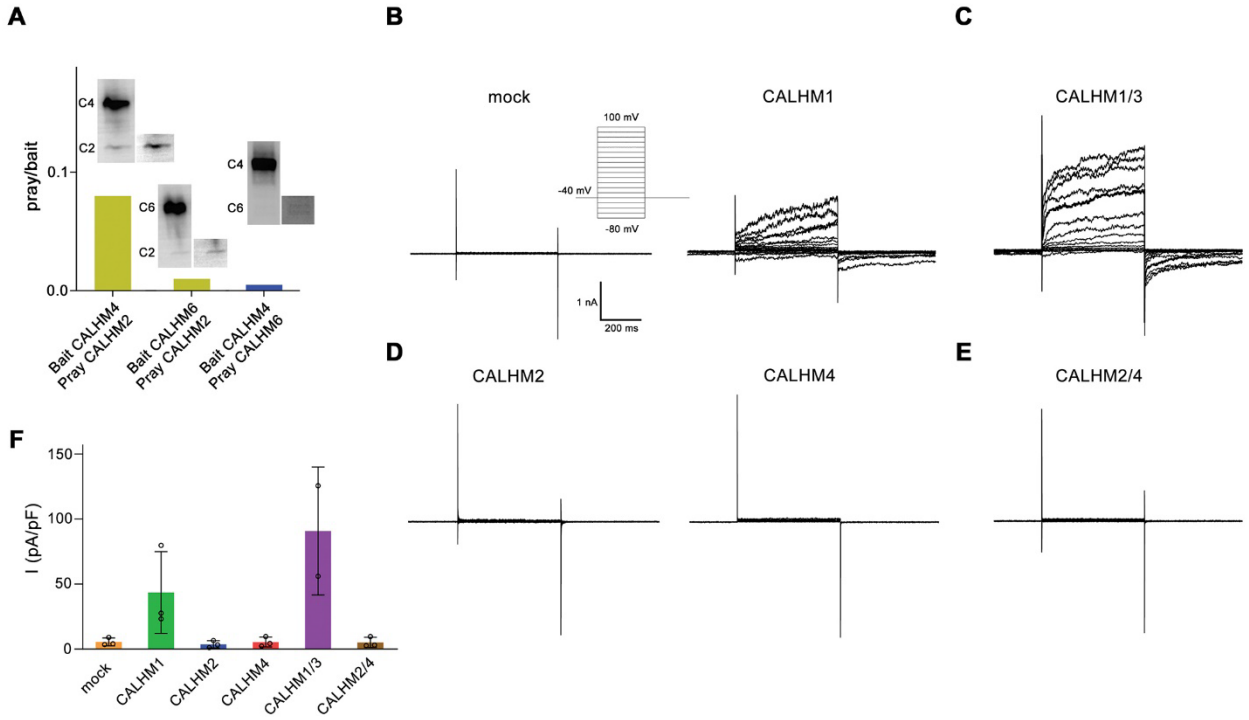

804

805 **Figure 1.** Heteromerization and functional properties of placental CALHM paralogs. (**A**) Western
806 blot (detecting the myc-tag attached to the C-termini of respective constructs) of CALHM subunits
807 expressed upon co-transfection of HEK293 GnTI⁻ cells with pairs of CALHM subunits. CALHM
808 channels were isolated by affinity purification of one subunit containing a fusion to Venus and an
809 SBP-tag (bait, shown at higher molecular weight). The resulting samples contain a mix of
810 homomers of the purified subunit and heteromers (with the second subunit not containing Venus
811 and SBP tags, prey at lower molecular weight). The ratio of pray/bait is displayed based on the
812 integration of the intensity of the displayed Western blots. The experiment has been carried out
813 once. (**B-E**) Represented patch-clamp electrophysiology recordings (whole cell configuration) of
814 indicated CALHM subunits expressed in HEK-293 cells measured in buffers containing 2 mM
815 Ca^{2+} on the extracellular side. (**B**) Comparison of currents from mock transfected cells (left) and

816 cells expressing CALHM1 (right). Inset shows voltage protocol. (**C**) Current response from cells
817 co-transfected with DNA coding for CALHM1 and CALHM3 subunits. (**D**) Current response
818 from cells transfected with CALHM2 (left) or CALHM4 (right) subunits. (**E**) Current response
819 from cells co-transfected with CALHM2 and CALHM4 subunits. (**F**) Mean current density of
820 recordings of different CALHM constructs (measured at 100 mV, 190 ms after the voltage step),
821 errors are s.e.m., values from individual recordings are shown as circles.

822

823 **Figure supplement 1.** Electrophysiology data of CALHM paralogs at low extracellular Ca^{2+}.

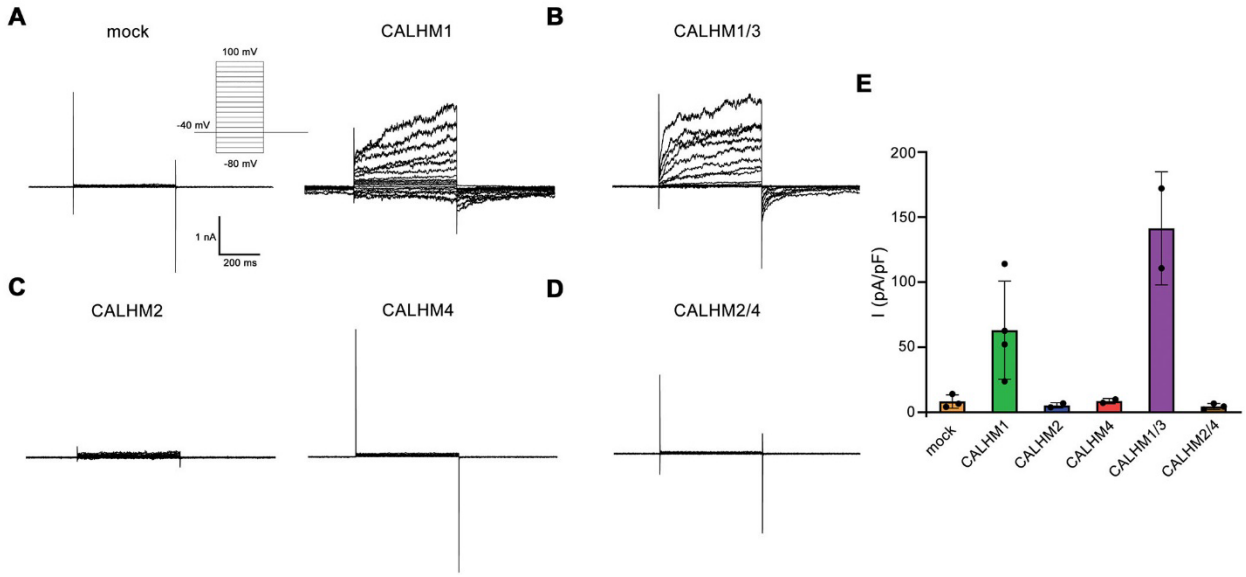

Figure 1—figure supplement 1. Electrophysiology data of CALHM paralogs recorded at low extracellular Ca^{2+}. (**A-D**) Patch clamp electrophysiology recordings (whole cell configuration) of representative traces of indicated CALHM subunits expressed in HEK-293 cells measured in buffers not containing Ca^{2+} on the extracellular side. (**A**) Comparison of currents from mock transfected cells (left) and cells expressing CALHM1 (right). Inset shows voltage protocol. (**B**) Current response from cells co-transfected with DNA coding for CALHM1 and CALHM3 subunits. (**C**) Current response from cells transfected with CALHM2 (left) or CALHM4 (right) subunits. (**D**) Current response from cells co-transfected with CALHM2 and CALHM4 subunits. (**E**) Mean current density of recordings of different CALHM constructs (measured at 100 mV, 400 ms after voltage step), errors are s.e.m., values from individual recordings are shown as circles.

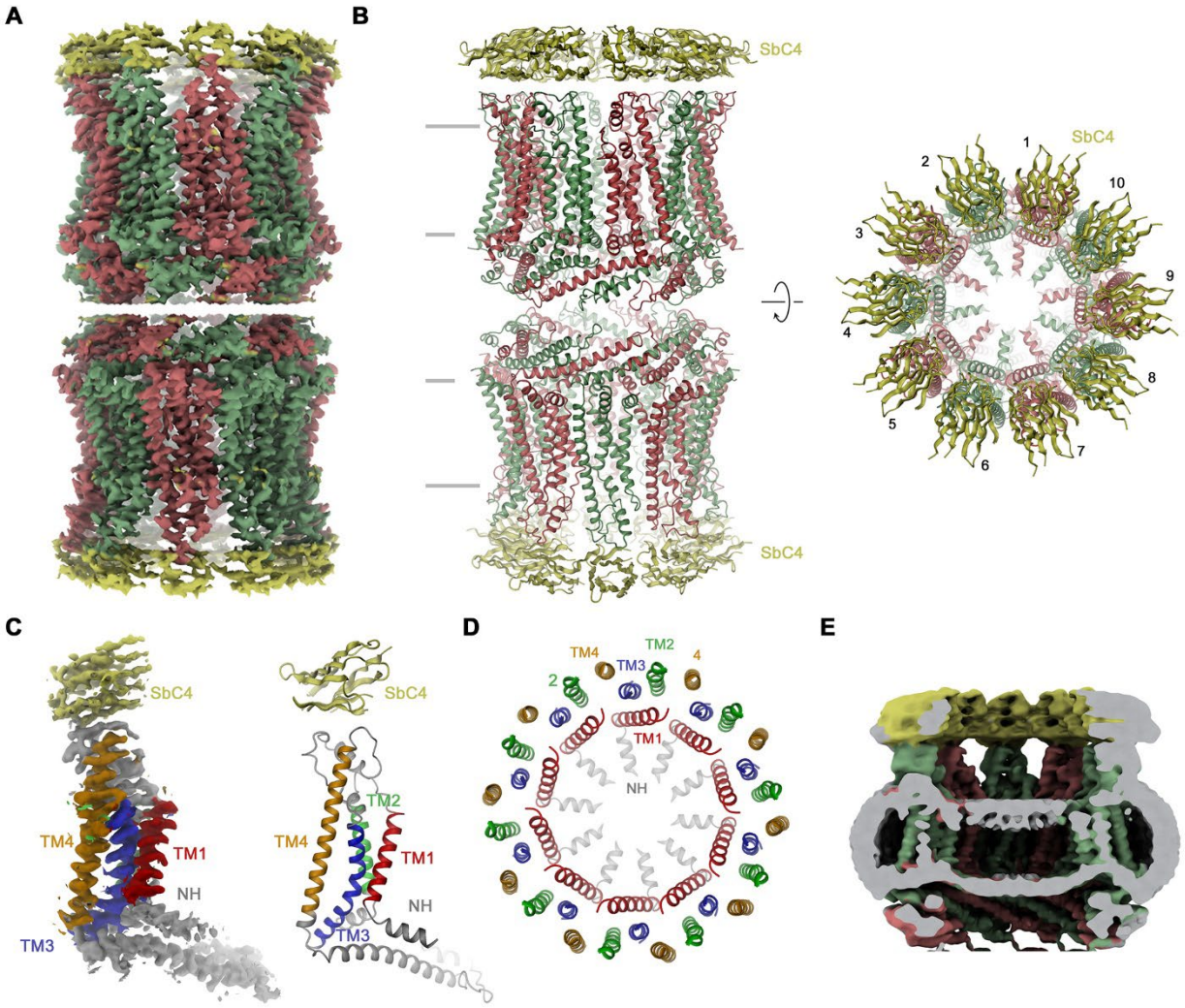

Figure 2. Structural characterization of the CALHM4/SbC4 complex. (**A**) Cryo-EM density at 3.7 Å (after application of D10 symmetry) of a pair of decameric CALHM4/SbC4 complexes interacting via their cytoplasmic regions. (**B**) Ribbon representation of the same complex viewed parallel (left) and perpendicular (right) to the membrane plane. Membrane boundaries are indicated (left). **A**, **B**, CALHM4 subunits are colored in red and green, SbC4 in yellow. (**C**) Cryo-EM density (left) and ribbon representation (right) of a single subunit of the CALHM4/SbC4 complex. Transmembrane helices are labeled and shown in unique colors. (**D**) Organization of TM helices in the decameric channel. The view is from the extracellular side, the coloring is as in C. (**E**) Slab

844 through a low-pass filtered map of the CALHM4/SbC4 complex (viewed from within the
845 membrane) shows bilayer-like density in the lumen of the wide pore.
846
847 **Figure supplement 1.** Sybody selection and characterization.
848 **Figure supplement 2.** Cryo-EM reconstruction of CALHM4 in complex with sybody SbC4.

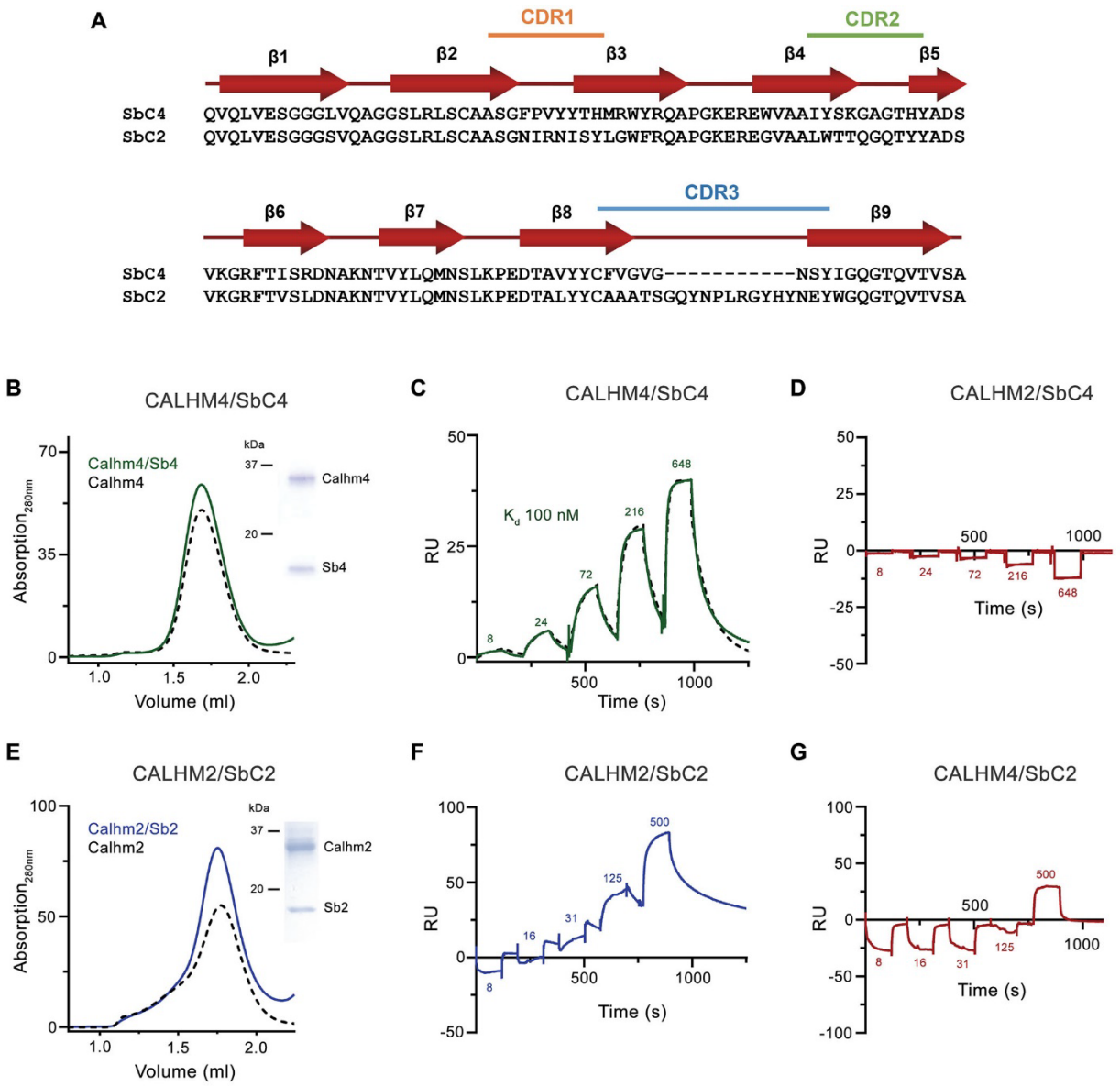

Figure 2—figure supplement 1. Sybody selection and characterization. (**A**) Sequence alignment of the two sybodies SbC4 and SbC2 specifically targeting CALHM4 and CALHM2, respectively. (**B**) Size exclusion chromatography profile of the CALHM4/SbC4 complex. The elution peak of the equivalent amount of CALHM4 is displayed as dashed line in comparison. Inset (right) shows SDS-PAGE gel of the peak fraction. SPR experiments of SbC4 binding to immobilized CALHM4 illustrating specific binding (**C**) and to CALHM2 not showing specific interactions (**D**). Dashed

856 line in D corresponds to a fit to a 1:1 binding model yielding a K_d of 100 nM. (**E**) Size exclusion
857 chromatography profile of the CALHM2/SbC2 complex. The elution peak of the equivalent
858 amount of CALHM2 is displayed as dashed line in comparison. Inset (right) shows SDS-PAGE
859 gel of the peak fraction. SPR experiments of SbC2 binding to immobilized CALHM2 illustrating
860 specific binding (**F**) and CALHM4 not showing specific interactions (**G**). B-G the experiments
861 werw carried out once.

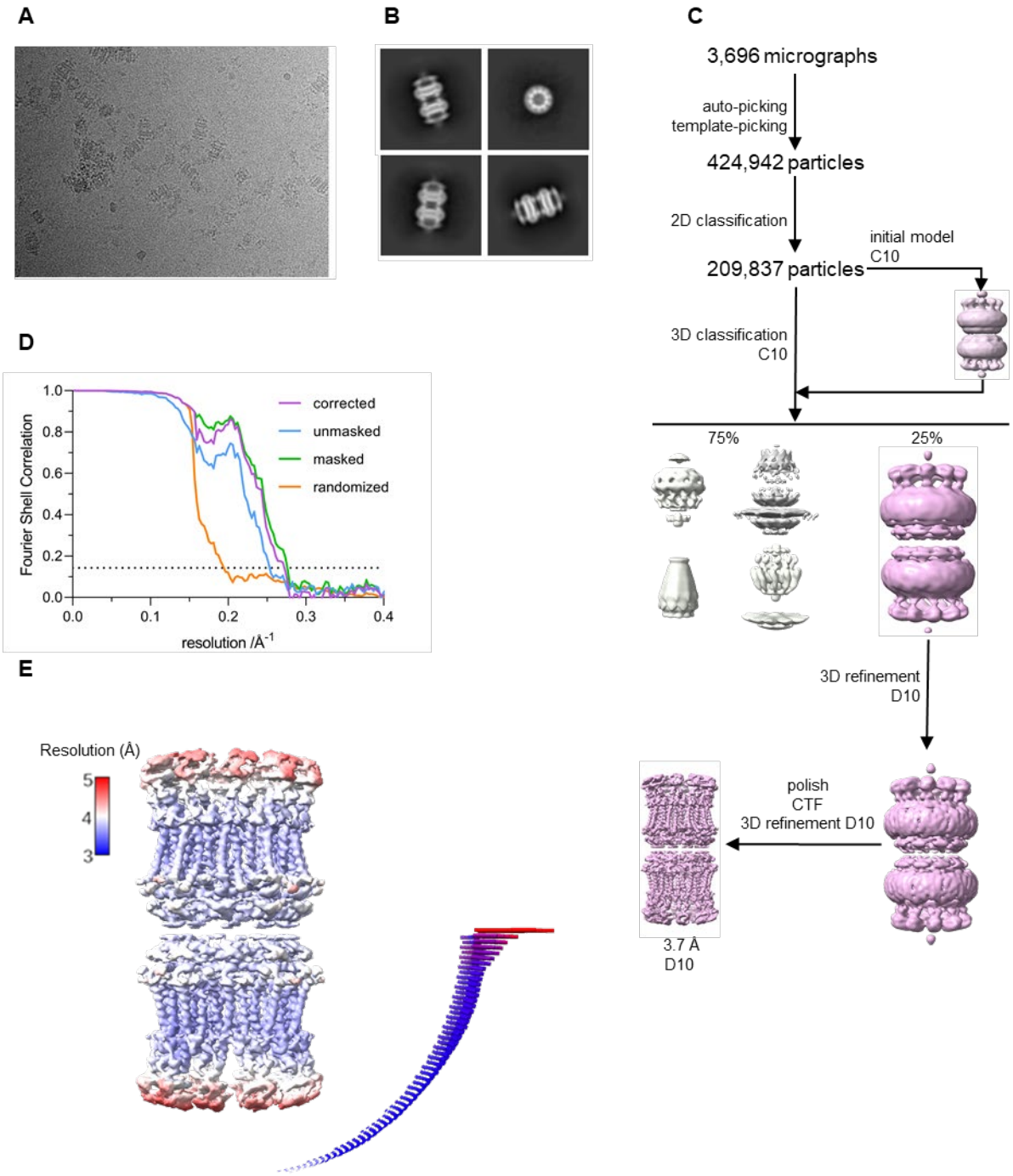

Figure 2—figure supplement 2. Cryo-EM reconstruction of CALHM4 in complex with sybody SbC4. (**A**) Representative cryo-EM micrograph acquired with a Titan Krios microscope equipped with a K3 camera. (**B**) Representative 2D class averages of the CALHM4/Sbc4 complex. (**C**) Data processing workflow. Particles were picked and subjected to 2D classification. High resolution 2D

class averages were used as input for initial 3D model generation and subsequent 3D classification. The 3D classification allowed to isolate CALHM4-SbC4 particles, which were further refined with iterative polishing, and 3D and CTF refinements. The distribution of particles (%) of each class is indicated. (**D**) FSC plot of the final refined undecameric unmasked (blue), masked (green), randomized (orange) and corrected for mask convolution effects (purple) cryo-EM density map of the CALHM4/SbC4 complex. The resolution at which the FSC curve drops below the 0.143 threshold is indicated. (**E**) Final 3D reconstruction of CALHM4/SbC4 complex colored according to local resolution. The angular distribution of the particles included in the final reconstruction is indicated. Each cylinder represents one view and the height corresponds to the number of particles in that view.

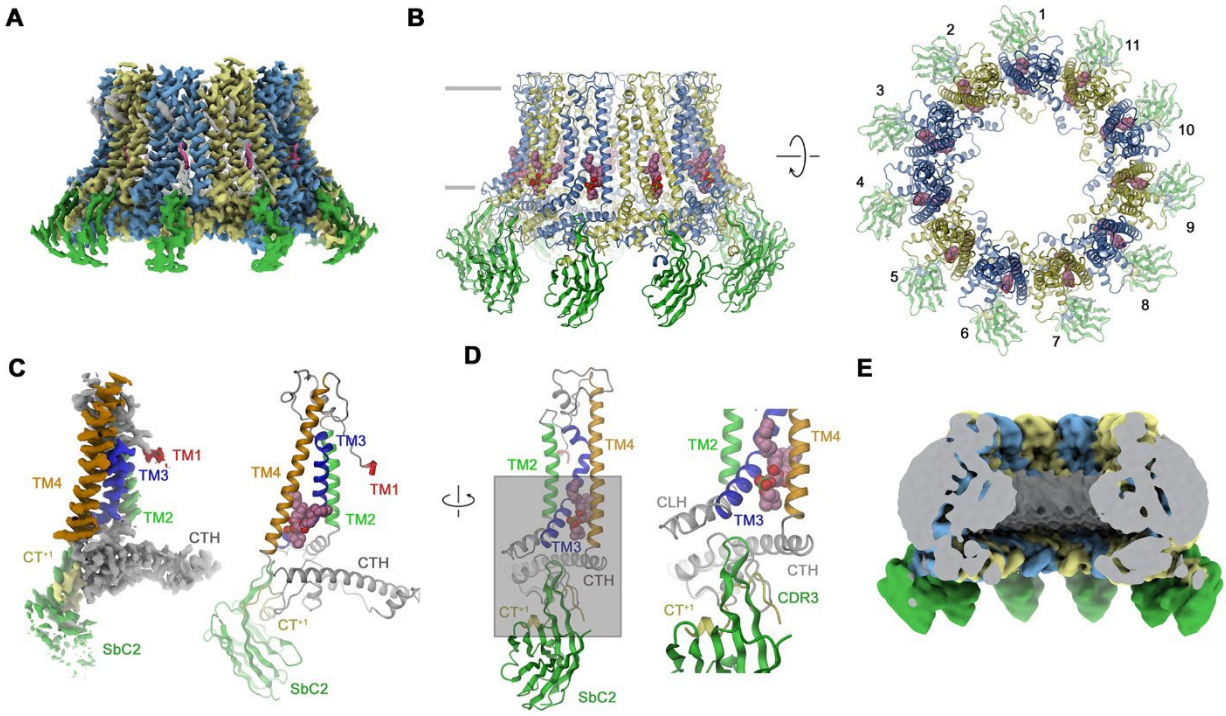

877

878 **Figure 3.** Structural characterization of a CALHM2/SbC2 complex. (**A**) Cryo-EM density of the
879 undecameric CALHM2/SbC2 complex at 3.1 Å (after application of C11 symmetry). (**B**) Ribbon
880 representation of the same complex viewed parallel to the membrane plane (left) and from the
881 extracellular side (right). Membrane boundaries are indicated (left). Space filling model shows a
882 bound lipid. **A**, **B**, CALHM2 subunits are colored in yellow and blue, SbC2 in green, the bound
883 lipid in magenta. (**C**) Cryo-EM density (left) and ribbon representation (right) of a single subunit
884 of the CALHM2/SbC2 complex. Transmembrane helices are labeled and shown in unique colors.
885 (**D**) Subunit (with orientation relative to C indicated) and blow-up of the sybody-interaction region.
886 The C-terminus of the adjacent subunits contributing to the interaction epitope is colored in yellow
887 and labeled (CT^{+1}). (**E**) Slab through a low-pass filtered map of the CALHM2/SbC2 complex
888 (viewed from within the membrane) does not show bilayer-like density in the lumen of the pore.

889

890 **Figure supplement 1.** Cryo-EM reconstruction of CALHM2 in complex with sybody SbC2.

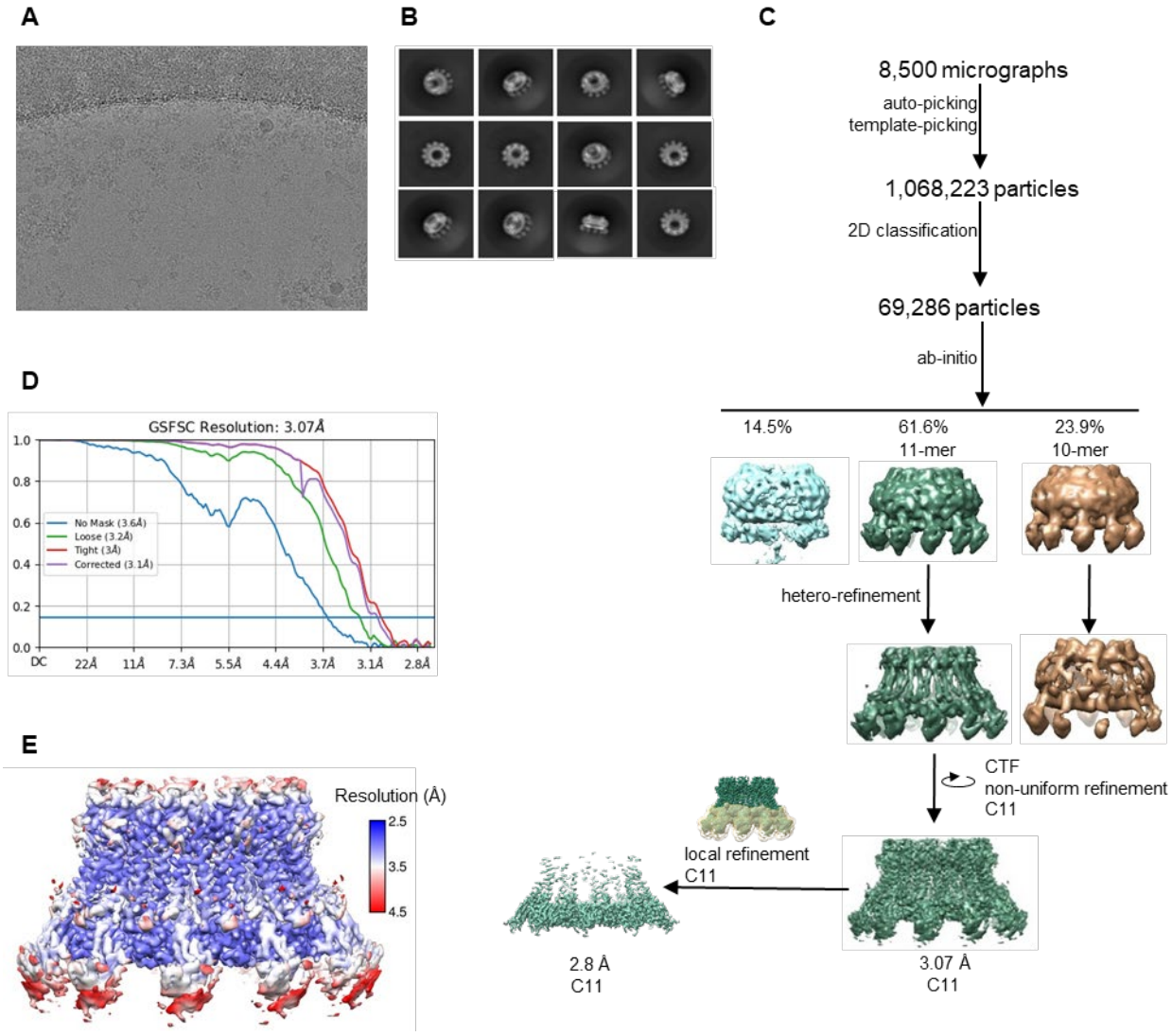

Figure 3—figure supplement 1. Cryo-EM reconstruction of CALHM2 in complex with sybody SbC2. (**A**) Representative cryo-EM micrograph acquired with a Titan Krios microscope equipped with an energy filter and a K3 camera. (**B**) 2D class averages of CALHM2-SbC2 complex. (**C**) Data processing workflow. Particles were picked and subjected to 2D classification. High resolution 2D class averages were used as an input for ab-initio reconstructions, which allowed to isolate two populations of particles (containing decameric and undecameric assemblies) from a decoy class. The distribution of particles (%) of each class is indicated. Particles were further sorted by heterogenous refinement and undecameric assemblies were improved in several rounds

900 of iterative non-uniform and CTF refinement. To increase the resolution in the sybody binding site,
901 a local refinement of the masked interaction region was performed. (**D**) FSC plot of the final
902 refined cryo-EM density map of undecameric channels (unmasked (blue), loose (green) and tight
903 (red) mask, and corrected for mask convolution effects (purple)) of the CALHM2/SbC2 complex.
904 The resolution at which the FSC curve drops below the 0.143 threshold is indicated. (**E**) Final 3D
905 reconstruction of the CALHM2/sybody complex colored according to local resolution.

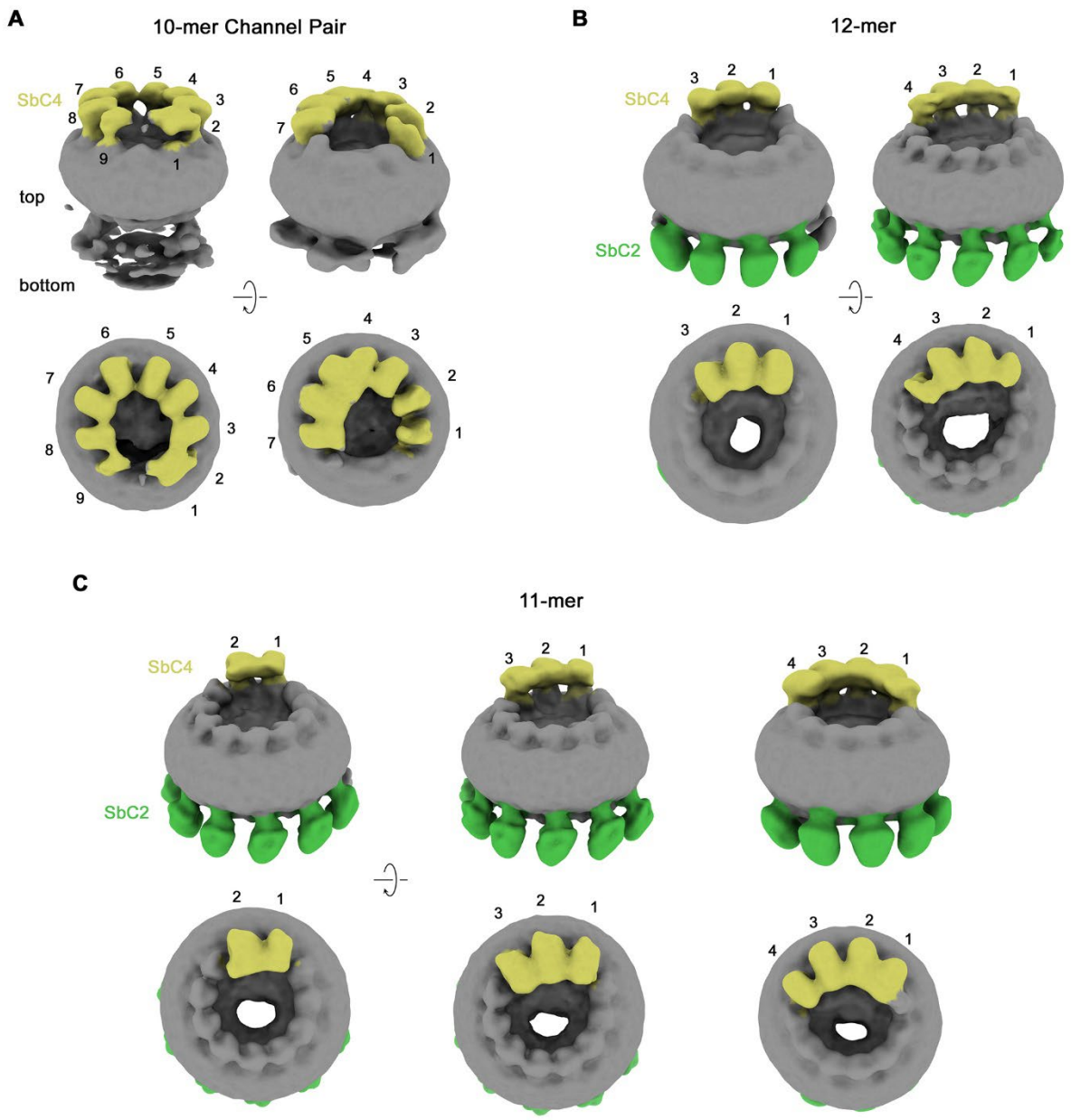

Figure 4. Classification of CALHM2/CALHM4 heteromers. Classes correspond to distinct populations of oligomers in the CALHM2/4/SbC2/SbC4 complex. (**A**) Assemblies containing an excess of CALHM4 subunits. Shown is the well-resolved halve of interacting channel pairs (with weak density corresponding to the second channel). (**B**, **C**) Assemblies with an excess of CALHM2 subunits. (**C**) Dodecameric channels containing three and four CALHM4 subunits. (**D**) Undecameric channels containing two to four CALHM4 subunits. **A-C**, Shown are low resolution

913 maps (processed in C1) with bound SbC2 and SbC4 colored in green and yellow , respectively.
914 Numbering refers to CALHM4 subunits. The relationship between views is indicated. Top panels
915 show inclined view towards the membrane plane, bottom panels a view from the extracellular side.
916
917 **Figure supplement 1.** Cryo-EM reconstruction of CALHM2/4 in complex with sybody SbC4.
918 **Figure supplement 2.** Cryo-EM reconstruction of CALHM2/4 in complex with sybodies SbC2
919 and SbC4.

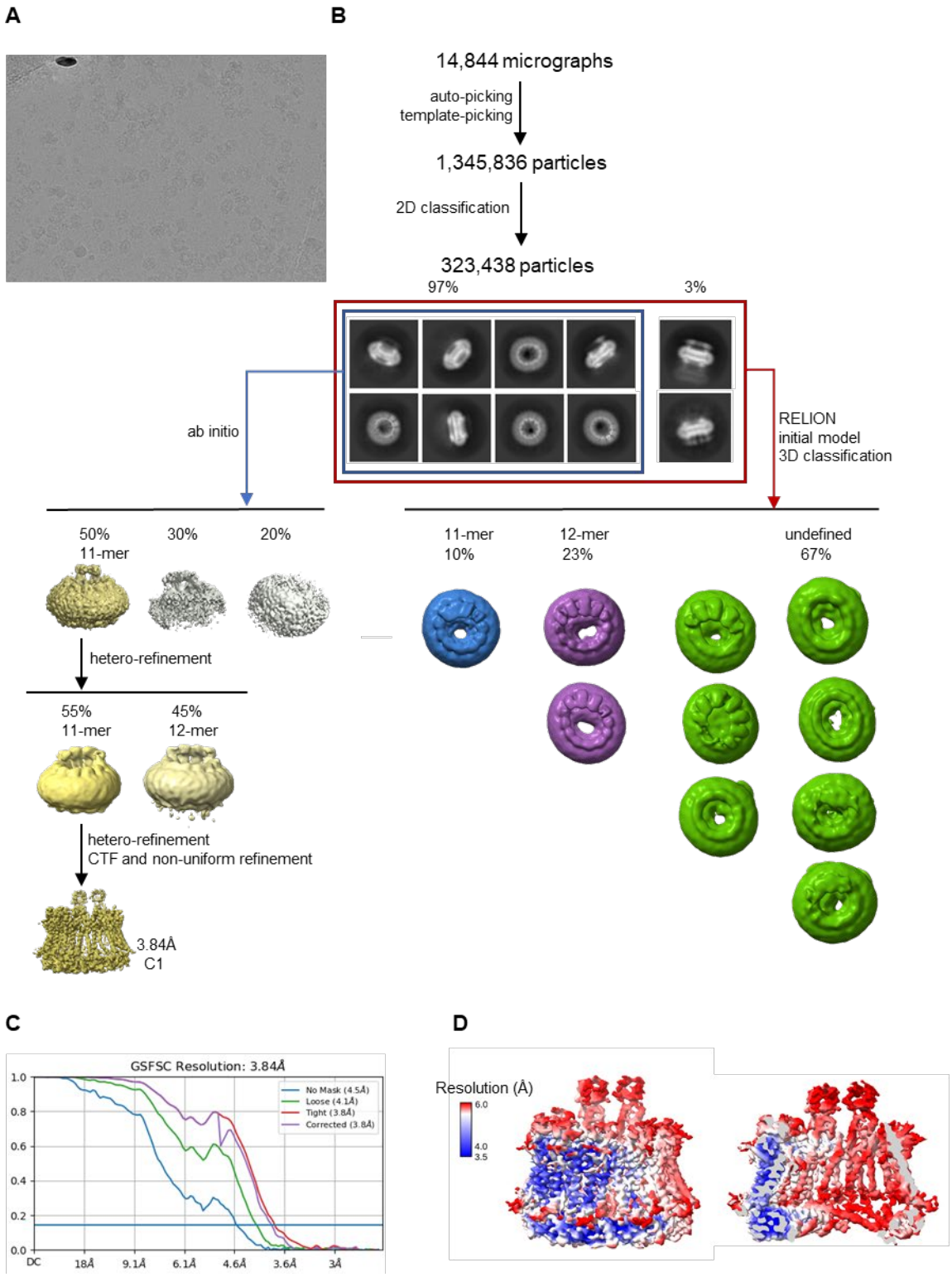

920

921 **Figure 4—figure supplement 1.** Cryo-EM reconstruction of CALHM2/4 in complex with sybody

922 SbC4. (**A**) Representative cryo-EM micrograph acquired with a Titan Krios microscope equipped

923 with a K3 camera. (**B**) Data processing workflow. Particles were picked and subjected to 2D
924 classification. 2D class averages allowed for the initial separation of populations of single
925 channels and their dimers. The distribution of particles (%) of each class is indicated. Further 3D
926 classification has led to the separation of different assemblies. Ab-initio reconstructions of particles
927 featuring single channels resulted in low resolution maps of undecameric assemblies. Further steps
928 of heterogenous refinement have separated undecamers and dodecamers. The smaller channels
929 were refined to high resolution via several cycles of hetero- and non-uniform refinement. (**C**) FSC
930 plot of the final refined unmasked (blue), masked (green), randomized (orange) and corrected for
931 mask convolution effects (purple) cryo-EM density maps of an undecameric CALHM4/SbC4
932 complex. (**D**) Final 3D reconstruction of a CALHM2/4/SbC4 complex colored according to local
933 resolution.

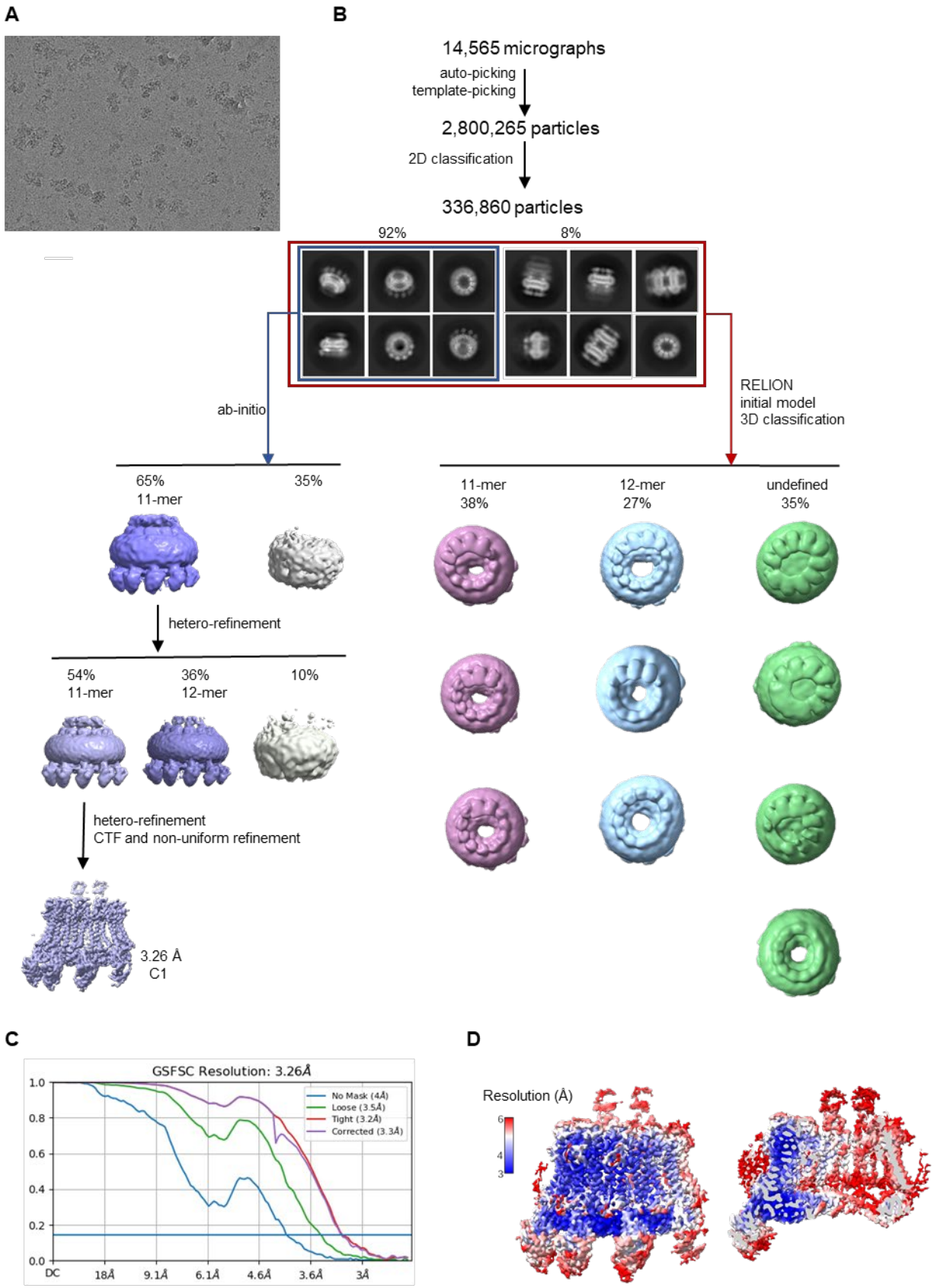
A
B
14,565 micrographs
auto-picking
template-picking
2,800,265 particles
2D classification
336,860 particles
92%
8%
ab-initio
RELION
initial model
3D classification
65%
11-mer
35%
hetero-refinement
54%
11-mer
36%
12-mer
10%
hetero-refinement
CTF and non-uniform refinement
3.26 Å
C1
11-mer
38%
12-mer
27%
undefined
35%
C
GSFSC Resolution: 3.26Å
No Mask (4Å)
Loose (3.5Å)
Tight (3.2Å)
Corrected (3.3Å)
1.0
0.8
0.6
0.4
0.2
0.0
DC
18Å
9.1Å
6.1Å
4.6Å
3.6Å
3Å
D
Resolution (Å)
6
4
3

934

935 **Figure 4—figure supplement 2.** Cryo-EM reconstruction of CALHM2/4 in complex with
936 sybodies SbC2 and SbC4. (**A**) Representative cryo-EM micrograph acquired with a Titan Krios
937 microscope equipped with a K3 camera. (**B**) Data processing workflow. Particles were picked and
938 subjected to 2D classification. High resolution 2D class averages revealed populations of single
939 channels and dimers of channels. The distribution of particles (%) of each class is indicated.
940 Subsequent 3D classification of all the particles allowed for the separation of different assemblies.
941 Ab-initio reconstructions of particles featuring single channels yielded undecameric assemblies.
942 The subsequent heterogenous refinement separated undecameric and dodecameric channels. The
943 undecameric assemblies were further improved to high resolution by hetero, CTF and non-uniform
944 refinement. (**C**) Fourier shell correlation (FSC) curves of the final refined unmasked (blue),
945 masked (green), randomized (orange) and corrected for mask convolution effects (purple) cryo-
946 EM density maps of an undecameric CALHM2/4/SbC2/SbC4 complex. (**D**) Final 3D
947 reconstruction of the CALHM2/4/SbC2/SbC4 complex colored according to local resolution.
948 Shown is the map of the channel viewed from the side (left) and the slice through the channel
949 (right).

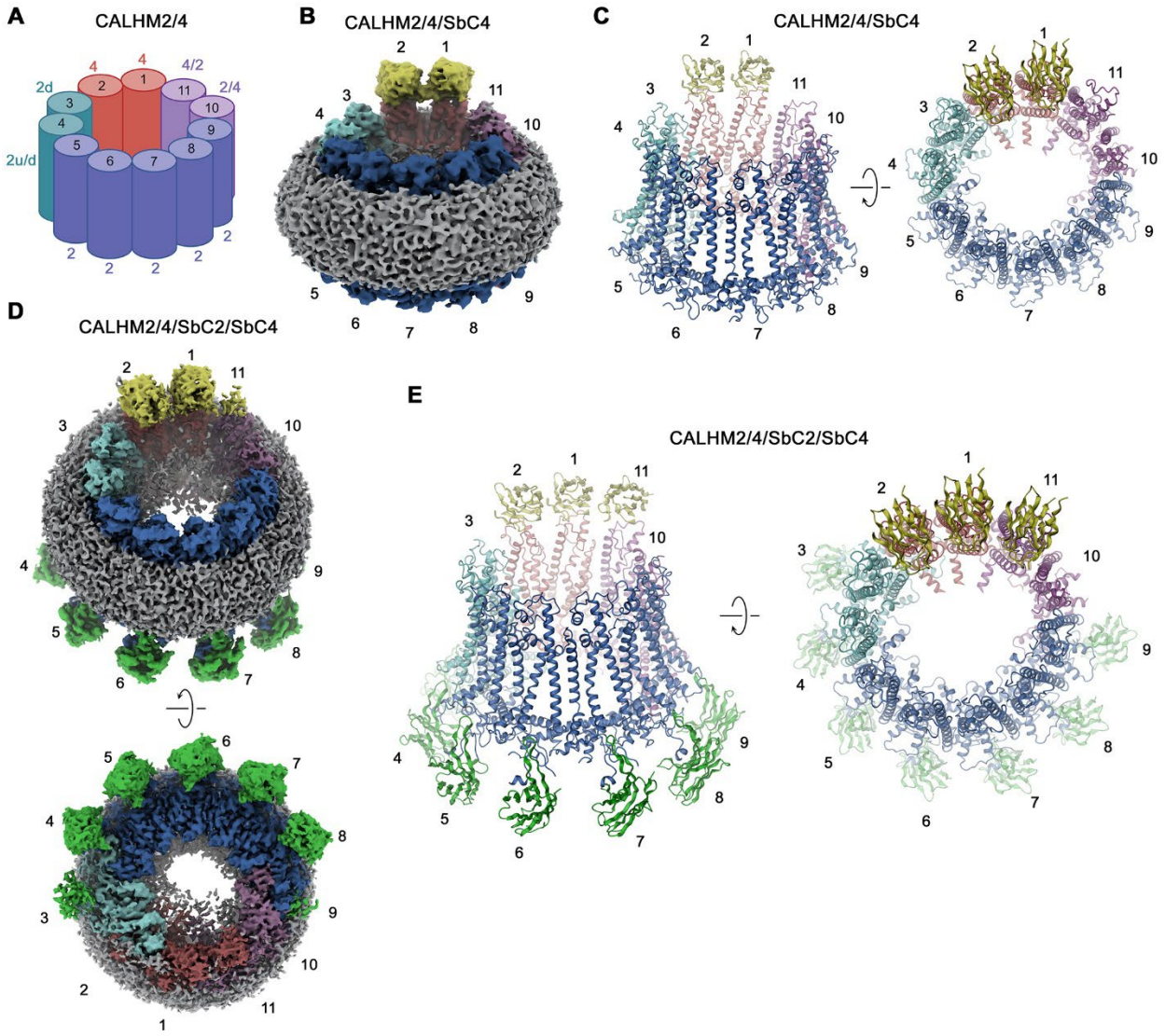

Figure 5. CALHM2/CALHM4 heteromer structure. (**A**) Schematic depiction of the subunit distribution in CALHM2/4 heteromers. 4 refers to CALHM4, 2 to CALHM2 in 'up' conformation, 2d to CALHM2 in 'down' conformation, 2u/d to a mixed population of both conformations of CALHM2 subunits, 4/2 and 2/4 to mixed populations of CALHM2 and 4 with the first number indicating the predominant subunit. (**B**) Cryo-EM density of the CALHM2/4/SbC4 complex at 3.8 Å viewed with an inclination towards the membrane plane. (**C**) Ribbon representation of the CALHM2/4/SbC4 complex viewed from the same perspective as in B (left) and from the extracellular side (right). (**D**) Cryo-EM density of the CALHM2/4/SbC2/SbC4 complex at 3.3 Å

959 viewed with an inclination towards the membrane plane (top) and from the intracellular side
960 (bottom). (**C**) Ribbon representation of the CALHM2/4/SbC2/SbC4 complex viewed from the
961 same perspective as in B (left, top) and from the extracellular side (right). **B**-**E**, Colors and numbers
962 of channel subunits are as in **A**. SbC2 and SbC4 are colored in yellow and green, respectively.

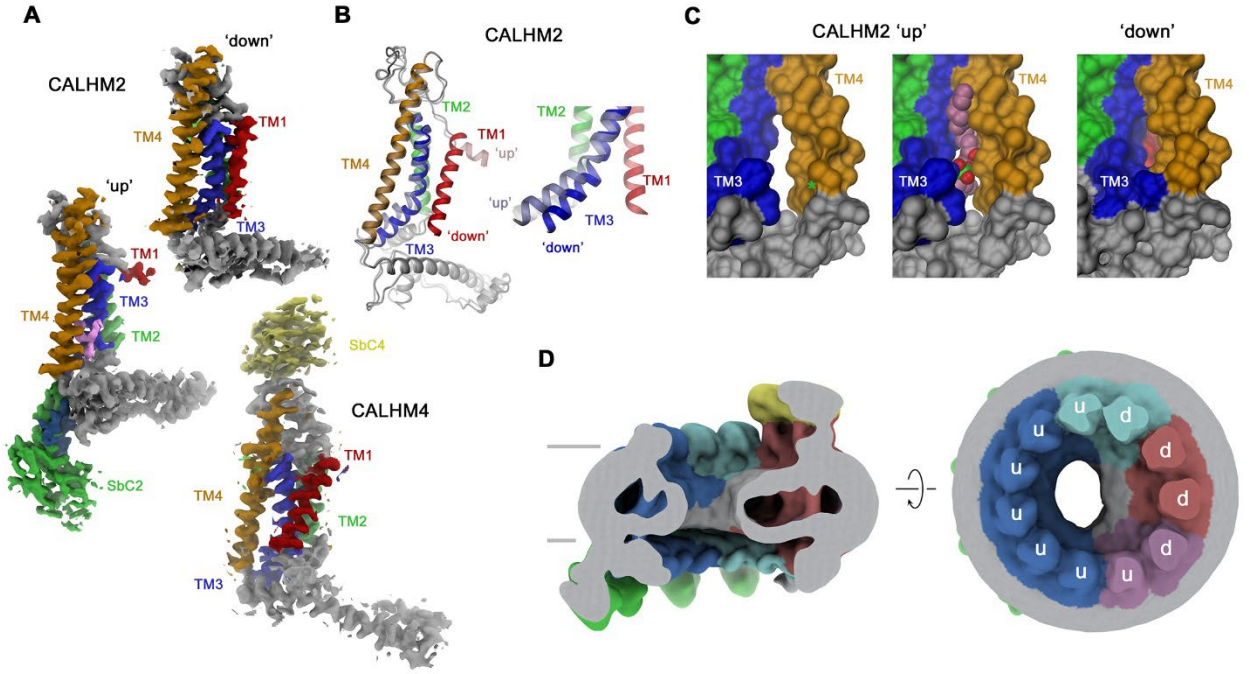

Figure 6. Conformational properties of CALHM subunits in CALHM2/4 heteromers. (**A**) Cryo-EM density of CALHM2 subunits in 'down' (position 3, left) and 'up' (position 6, top) and of CALHM4 (in 'down' conformation, position 1, bottom). (**B**) Ribbon representation of a superposition of CALHM2 subunits in 'up' and 'down' conformations. Inset (right) shows blowup of the intracellular region around TM1-3. (**C**) Molecular surface of the intracellular region relating TM3 and TM4 viewed from within the membrane plane. A gap between both helices (left, asterisk), which is occupied by a lipid (space-filling representation) in the 'up' conformation (center), is closed in the 'down' conformation (right). **A-C** Transmembrane helices and attached sybodies are shown in unique colors. (**D**) Low-pass filtered map of the CALHM2/4/SbC2/SbC4 complex depicting residual bilayer-like density in the pore lumen. Slice through the channel in a view parallel to the membrane (left), and from the extracellular side (right). Subunit conformations are indicated (d, 'down', u, 'up'). CALHM4 subunits are shown in red and magenta, CALHM2 subunits in blue and cyan.

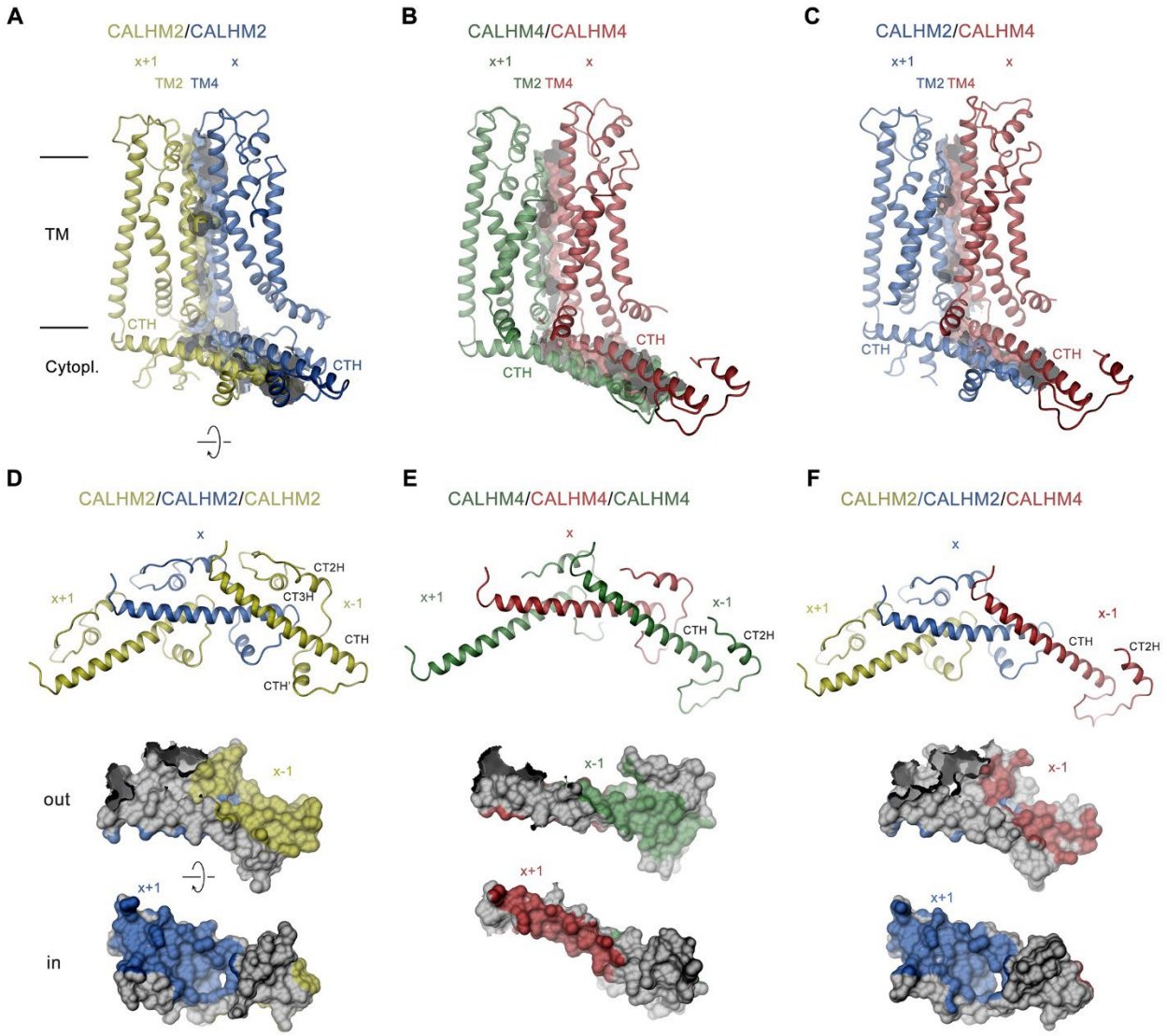

Figure 7. Structural features of subunit interfaces. (**A**-**C**) Interaction interfaces between pairs of CALHM2 subunits (**A**), CALHM4 subunits (**B**) and a CALHM2 and a CALHM4 subunit (**C**). Shown are ribbon representations of neighboring subunits viewed from the inside of the channel parallel to the membrane and their molecular surfaces that are buried in the interaction interface. (**D**-**F**) Subunit interactions in the cytoplasmic domain of CALHM channels. Shown is a central subunit (x) and its interaction partners in clockwise and counterclockwise position (top). The region of the intracellular domain that is contacted by neighboring subunits is mapped on the

986 molecular surface of the central subunit. Center, view from the extracellular side (out), bottom
987 from the cytoplasm (in). **A-F** The relative position of subunits within the assembly is indicated.
988 Paralogs are represented in unique colors.

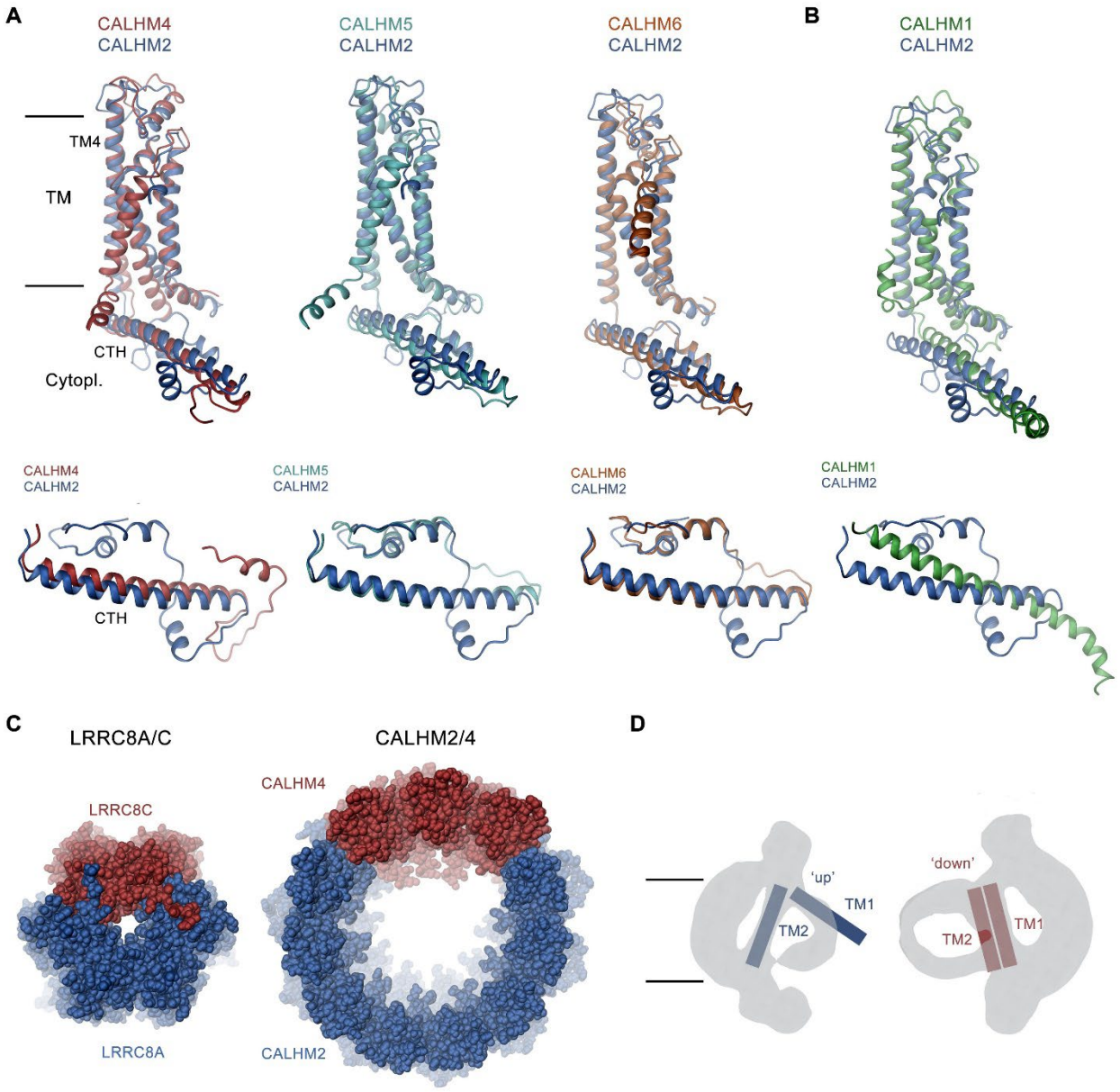

Figure 8. Discussion. (**A**, **B**) Superposition of single subunits of different CALHM paralogs on CALHM2 viewed from within the membrane (top) and of their cytosolic domain viewed from the outside (bottom). (**A**) Superposition with CALHM2-like subunits CALHM4-6. (**B**) Superposition with CALHM1. The difference in the conformation of the intracellular domain is apparent. (**C**) Segregation of subunits in heteromeric channels of the LRRC8 family (left) and of CALHM2/4 channels (right). Proteins are shown as space-filling models. The view is from the extracellular

996 side. (**D**) Schematic depiction of how the conformation of CALHM subunits influences the
997 properties of the bilayer-like density inside the channel. The conformation of helices is indicated.

998 **Table 1.** Cryo-EM Data collection, refinement and validation statistics.

	CALHM4/SbC4	CALHM2/SbC2	CALHM2/CALHM4/SbC4	CALHM2/CALHM4/SbC2/SbC4
	EMD-19365 PDB 8RMN	EMD-19362 PDB 8RMK	EMD-19363 PDB 8RML	EMD-19364 PDB 8RMM
Data collection and processing				
Microscope	FEI Titan Krios G3i	FEI Titan Krios G3i	FEI Titan Krios G3i	FEI Titan Krios G3i
Camera	Gatan K3+GIF	Gatan K3+GIF	Gatan K3+GIF	Gatan K3+GIF
Magnification	130,000	130,000	130,000	130,000
Voltage (kV)	300	300	300	300
Electron exposure (e^{-}/Å^2)	70	72	60	60
Defocus range (μm)	-1.0 to -2.4	-1.0 to -2.4	-1.0 to -2.4	-1.0 to -2.4
Pixel size* (Å)	0.651 (0.3255)	0.651 (0.3255)	0.651 (0.3255)	0.651 (0.3255)
Initial particle images (no.)	424,942	1,068,223	1,345,836	2,800,265
Final particle images (no.)	52,248	37,894	131,652	93,191
Symmetry imposed	D10	C11	C1	C1
Map resolution (Å) FSC threshold 0.143	3.7	3.07	3.84	3.26
Map resolution range (Å)	3.5-5	2.6-5	3.5-6	3-6
Refinement				
Model resolution (Å) FSC threshold 0.5	3.9	3.2	4.1	3.7

Map sharpening b-factor (Å^2)	-152.97	-101.8	-113.8	-67.2
Model composition Non-hydrogen atoms Protein residues Ligand (PLC)	55,460 7199	36,113 4521 11	24,456 3089 0	32,891 4163 6
B factors (Å^2) Protein Ligand	74.47	75.52 59.93	121.74	69.29 80.08
R.M.S. deviations Bond lengths (Å) Bond angles (°)	0.004 0.710	0.003 0.611	0.004 0.596	0.003 0.671
Validation MolProbity score Clashscore Poor rotamers (%)	2.00 13.63 1.16	1.86 12.04 0.45	1.87 12.92 0.46	1.85 11.37 0.79
Ramachandran plot Favored (%) Allowed (%) Disallowed (%)	95.60 4.40 0.00	96.05 3.95 0.00	96.28 3.72 0.00	96 3.98 0.02

*Values in parentheses indicate the pixel size in super-resolution.